Plasma flow measurements based on charge exchange recombination spectroscopy in the Wendelstein 7-X stellarator

J A Alonso[1], O P Ford[2], L Vanó[2], S Äkäslompolo[3], S Buller[2], R McDermott[4], H M Smith[2], J Baldzuhn[2], C D Beidler[2], M Beurskens[2], S Bozhenkov[2], K J Brunner[2], I Calvo[1], D Carralero[1], A Dinklage[2], T Estrada[1], G Fuchert[2], J Geiger[2], J Knauer[2], A Langenberg[2], N A Pablant[5], E Pasch[2], P Zs Poloskei[2], J L Velasco[1], T Windisch[2] and the W7-X team

[1]Laboratorio Nacional de Fusión, CIEMAT, 28040 Madrid, Spain
[2]Max-Planck-Institut für Plasmaphysik, 17489 Greifswald, Germany
[3]Aalto University, 02150 Espoo, Finland
[4]Max-Planck-Institut für Plasmaphysik, 85748 Garching, Germany
[5]Princeton Plasma Physics Laboratory, 08543 New Jersey, USA

E-mail: `arturo.alonso@ciemat.es`

Abstract. The initial operation of neutral beams in Wendelstein 7-X enabled the first measurements of carbon (C^{6+}) temperature and rotation with a multi-chord Charge eXchange Recombination Spectroscopy system. In this article we analyse the velocity measurements obtained with this system to infer the profiles of radial electric field, E_r, and net parallel velocity of fully stripped carbon ions, $V_\parallel$. We include a general treatment of the flow geometry and the velocity corrections due to the energy dependence of the charge exchange cross section. The inverted profiles are compared with neoclassical calculations for various plasma conditions and two magnetic configurations. It is found that both the E_r and $V_\parallel$ experimental profiles agree in sign and order of magnitude with the neoclassical expectations and reproduce the expected dependencies on plasma parameters and magnetic configuration, within the reduced dataset presented. However, quantitative differences with respect to the neoclassical profiles are observed above the estimated errors in various conditions.

Figure 1. Flow pattern in a Wendelstein 7-X flux surface. Black lines depict the stream lines while the color indicates the local speed of fully stripped carbon ions. The usual W7-X magnetic field direction (ccw seen from the top) is assumed. The radial electric field and net parallel velocity values correspond approximately to those found in the discharge 20180920.017 (see figure 10) at $\rho = 0.7$. The definition of the surface label ρ and the relation of E_r and $V_\parallel$ with the local fluid velocity can be found in Appendix A.

1. Introduction

At the time of writing this article, the Wendelstein 7-X (W7-X) stellarator has run one limiter and one divertor campaign, producing a wealth of experimental results [see e.g. 23, 43]. In the second half of the latter, first neutral beam injections (NBI) have been performed with injected powers up to 3.1 MW and accelerating voltage and beam current approaching the nominal design values [37]. Besides initial studies of the properties of NBI-heated plasmas and the verification of fast ion particle losses [25], NBI injections have allowed active spectroscopy to commence in W7-X. In [16], the first ion temperature and velocity measurement on fully ionised carbon are presented together with technical description of the Charge eXchange Recombination Spectroscopy system (CXRS) implemented in W7-X. In the present work we present the details of the analysis of the velocity data to obtain inverted profiles of the radial electric field, E_r, and net parallel velocity, $V_\parallel$. Under common and reasonable assumptions that we will later discuss, the fluid velocity of a high-Z plasma species at any point within a flux surface is determined only by the numerical values of E_r and $V_\parallel$ on that surface. This is exemplified in figure 1 for a W7-X surface. The problem at hand is then to combine multiple spectroscopic velocity measurements at various points and directions to find the E_r and $V_\parallel$ profiles that best reproduce the individual measurements.

In non-symmetric toroidal magnetic fields, the radial electric field and net parallel flow or 'rotation' are expected to be determined by the neoclassical collisional transport through ambipolarity and parallel momentum conservation. That is, given a set of plasma temperature and density profiles for the relevant plasma species and a magnetic equilibrium, the solution of the drift kinetic equations, together with
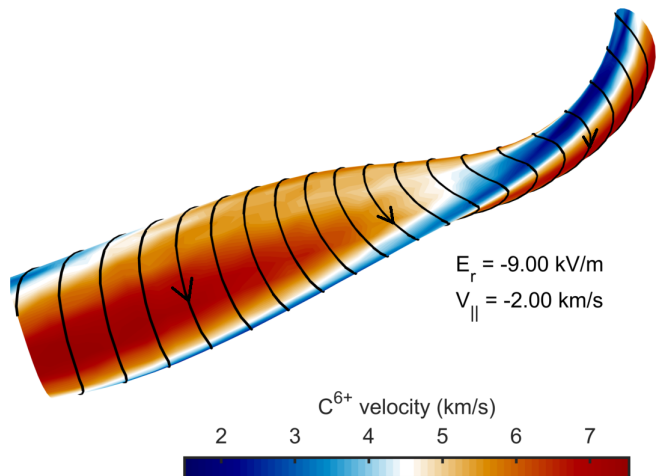
the ambipolarity constraint $\langle \mathbf{j} \cdot \nabla r \rangle = 0$ determines both the radial electric field and the parallel velocity of the species. The ambipolarity condition can be traced back to quasineutrality in the form $\nabla \cdot \mathbf{j} = 0$, which is expected to be well satisfied for transport-relevant spatial and temporal scales. In non-symmetric stellarators, the neoclassical radial particle fluxes are a strong function of the radial electric field (see e.g. figure 2), due to its profound influence on ion orbits. It is therefore difficult to identify any other current (e.g. as those driven by turbulence, fast ions or neutral friction) that can cause the radial electric field to substantially deviate from its neoclassical ambipolar value. The experimental verification of the neoclassical E_r and $V_\parallel$ profiles can, in this sense, be considered a partial validation of the neoclassical description of plasma transport in Wendelstein 7-X, whose optimisation targeted specific neoclassical quantities such as the effective ripple and the bootstrap current [18]. Furthermore, the radial electric field profile itself influences neoclassical as well as turbulent transport of particles and energy, so that its experimental determination bears a rather general importance for understanding transport processes in a stellarator. For their part, the net parallel velocities of the various plasma species determine the parallel bootstrap current, which is of particular importance for the magnetic equilibrium of a low-shear device like W7-X, with an island divertor configuration that requires a precise value of the edge rotational transform.
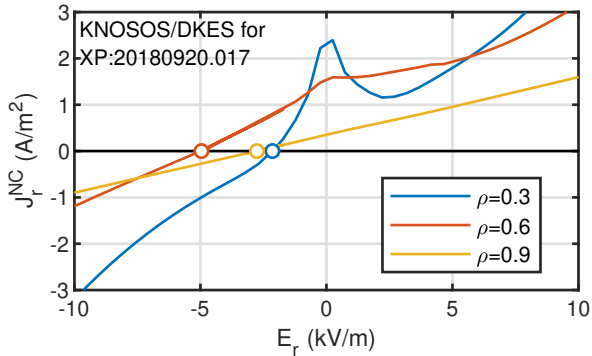
A review of previous comparisons between flow

Figure 2. Neoclassical radial current as a function of the radial electric field as calculated with KNOSOS/DKES (a database of DKES monoenergetic coefficients is convoluted with a Maxwellian distribution and, at low collisionalities, DKES coefficients are replaced with KNOSOS calculations, as discussed in [39]). Calculations for three magnetic surfaces for the equilibrium and profiles of discharge 20180920.017 (see figure 15) are shown. The circles correspond to the ambipolar electric field $j_r^{NC}(E_r) = 0$.

measurements (including data from CXRS, Doppler reflectometry and HIBP diagnostics) and expectations in stellarator devices cast a somewhat ambiguous picture as to the ability of neoclassical theory to reproduce the measurements [4, 10, 2, 13, 32, 26]. In most cases the qualitative agreement in the radial electric field is good, but factor of two differences are not uncommon. Parallel velocity measurements tend to capture the in-out Pfirsch-Schlüter flow pattern [2, 27, 44] which has even been used to infer the radial electric field from observations of paralllel flow at both sides of the magnetic axis [27]. Deviations from the Pfirsch-Schlüter pattern have been reported in collisional NBI plasmas in the TJ-II stellarator [1] and in tangential NBI plasmas of the LHD heliotron [44]. Furthermore, the LHD has also reported non-neoclassical or spontaneous *toroidal* flow [32].

Complementing previous investigations of the radial electric field in W7-X [42, 24, 33, 11, 15], in the present work we compare measured E_r profiles with neoclassical expectations and extend this comparison to the net parallel velocity. A good agreement between the experimental and neoclassical profiles is found in the order of magnitude and sign as well as in several qualitative features (root transitions, small central values for E_r and $V_\parallel$) and dependencies on magnetic configuration and plasma conditions. In interpreting the velocities, particular attention is given to the correct treatment of the flow geometry (Appendix A) and wavelength shifts due to atomic physics corrections (Appendix B). The importance of considering a realistic flow geometry for interpreting the spectroscopy velocity measurements has been illustrated in several stellarator devices [2, 26, 44]. The

atomic physics corrections, on the other hand, have not become necessary for the interpretation of the velocity measurements in devices with low ion temperature and have only recently been investigated in the LHD device [12]. As we will show, those corrections produce sizeable changes of the measured velocities that result nevertheless in moderate quantitative changes of the inverted velocity profiles. Considering them generally improves their agreement with the theoretical neoclassical expectations, but there remain quantitative differences above the estimated errors.

The paper is organised as follows: section 2 presents the modelling of the neutral beam that is required for the interpretation of the CXRS signal and the calculation of some velocity corrections. In section 3 the results of the flow inversions for several W7-X plasma conditions are presented and compared to the neoclassical calculations. Section 4 contains a discussion of the measurements in relation to other diagnostics and possible causes of the deviations with respect to neoclassical observations. The main conclusions are summarised in section 5. Technical aspects of flow geometry and velocity corrections are relegated to the appendices.

2. Beam modelling for velocity correction

Active carbon charge exchange (CX) spectroscopic measurements at W7-X rely on the reaction

$$C^{6+} + H^0 \rightarrow C^{5+}(n = 8 \rightarrow 7) + H^+ , \tag{1}$$
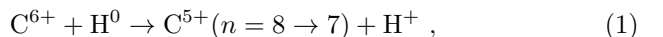
between the fully stripped carbon ions present in the plasma and the high-energy beam neutrals. The cross section of this process has a peak around 60 keV/amu (see figure 3). The resulting excited C^{5+} ion has a high probability of being in an $n = 8$ energy state and rapidly decaying into $n = 7$, emitting a photon of 529 nm wavelength. The acceleration voltage of W7-X neutral beams is around 60 kV, which is particularly suited to the use of this line for diagnostic purposes. The energy dependence of the cross-section shown in figure 3 results in a distortion of the excited C^{5+} charge exchange distribution function relative to that of the receiving C^{6+} ion species. For high-T_i plasmas, this translates into a spurious shift and broadening of the spectral line that affect their interpretation as fluid velocity and temperature [21, 20, 7]. In Appendix B we derive the expressions for the apparent velocities used in this article. As it is also shown there, ion temperature corrections are not important for the W7-X conditions.

To implement the corrections to the measured velocity one needs to be able to estimate the relative size of the several contributions to the reaction (1) that are produced by the neutral beam injection. The neutral hydrogen H^0 donor can belong to the full,
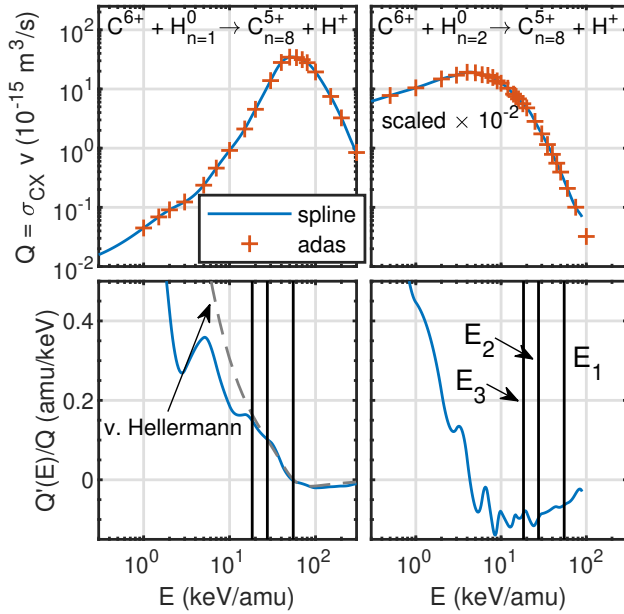
Figure 3. Energy dependence of $\sigma_{CX}v$ for the CX reaction between a hydrogen donor atom in its ground (left) and first energy level $n = 2$ (right) and fully ionised carbon ion (data from https://open.adas.ac.uk/). The lower plots show the logarithmic derivative of $\sigma_{CX}v$ that is relevant for the correction of the C^{6+} velocities inferred from the CXRS measurements. The vertical bars indicate the typical energies of the beam components in the W7-X shots analysed in this work. The logarithmic derivative of the $n = 1$ cross section agrees well with von Hellermann's analytic approximation [20] in the energy range of relevance for neutral beams. Second order derivatives (not shown in these plots) enter temperature corrections. For reference, for charge exchange with ground state hydrogen neutrals (left), $EQ''(E)/Q(E) \sim -0.1$ amu/keV at the peak Q.

half or third energy component of the beam or to the so-called beam *halo*. Halo neutrals are created by charge exchange between beam neutrals and thermal main ions. Its contribution to the CXRS signal is dominated by the small excited population in the first excited energy level ($n = 2$), which exhibits a large CX cross section with C^{6+} ions (see figure 3 right). In this section we show that, for the conditions found at W7-X, the leading contributions to the active $C^{5+}(n = 8 \to 7)$ line signal are the electron capture from the ground state neutrals of the full and half energy components of the beam and from the excited $n = 2$ halo neutrals. Similar conditions are found in, e.g., the ASDEX upgrade tokamak [31].

The initial energy composition of the neutral beam is obtained from spectroscopic measurements in the beam neutraliser whereas the attenuation of each component is computed from the effective beam stopping coefficients that depend on the beam energy and the plasma parameters along the beam. To estimate the relative halo density we assume a stationary balance of the electron impact ionization

of the halo neutrals and the creation of new halo particles by CX reactions between thermal ions and beam neutrals, i.e.

$$n_e n_b^{halo} \langle \sigma_{ion} v \rangle = n_i n_b V_b \sigma_{CX}(V_b) \ . \tag{2}$$

In this expression n_e and n_i are the electron and main ion densities, n_b and V_b are the density and velocity of the particular neutral beam energy component ($b \in [1, 2, 3]$ labels respectively the full, half and third energy components). The cross sections in (2) correspond to the electron impact ionization (σ_{ion}), and the charge exchange reactions between beam neutrals H^0 and plasma H^+ ions (σ_{CX})‡. Convolution with the Maxwellian distribution is considered for the electrons on the LHS of this equation but is neglected for ions on the RHS since they are effectively at rest with respect to the beam neutrals (see Appendix C). If one neglects direct losses of CX neutrals, this balance must hold in stationary state in a volume-integrated sense. The assumption made here is that the balance holds locally within the observation volume of each CXRS chord. Figure 4 shows the resulting ground-state beam and halo densities along the beam path (blue lines in the three lower plots). The halo-to-beam ratio peaks at the center were the larger T_e results in a lower ionization rate (see figure 5). These ground state populations are excited by collisions with the plasma electrons. An estimation of the excited $n = 2$ density fraction that is present in the beam and halo populations (red lines in the lower plots of figure 4) can be obtained from the local balance of the main sources of excited neutral (electron and proton impact excitation) and the main depleting mechanism (radiative decay), i.e.

$$n_0^{(1)} \left(n_e \langle \sigma_{e-\text{imp}}^{1\to 2} v \rangle + n_i \langle \sigma_{i-\text{imp.}}^{1\to 2} v \rangle \right) = \gamma^{2\to 1} n_0^{(2)} \ . \tag{3}$$

The cross sections can be found in e.g. [22]. This approximation neglects the population of the $n = 2$ state by radiative decay from higher excited states as well as its depletion by excitation, ionization or charge exchange processes, which are more important at high densities. Some of these effects are accounted for by using the ADAS photo emission coefficients (PEC) derived from a full collisional-radiative model. Use of these PEC results in relatively small ($\lesssim 15\%$) differences in the estimated $n = 2$ population compared to the one given by (3) with the value recommended in [41] for the transition probability $\gamma^{2\to 1} = 4.70 \times 10^8$ s^{-1}.

The combination of the relative neutral densities along the beam path (figure 4) and the reaction rates

‡ To keep notation simple, we use the same symbol, σ_{CX}, as we used in figure 3 to denote the cross section of the charge exchange between and neutral hydrogen atom and a C^{6+} ion. It should be clear from the context which ion (H^+ or C^{6+}) is participating in the electron capture.

Figure 5. Ionization rate of neutral hydrogen by electron impact (blue) and $H^+ + H^0$ charge transfer (red) derived from the cross section recommended in [22]. Electron impact ionization is convolved with a Maxwellian electron distribution with temperature T_e.
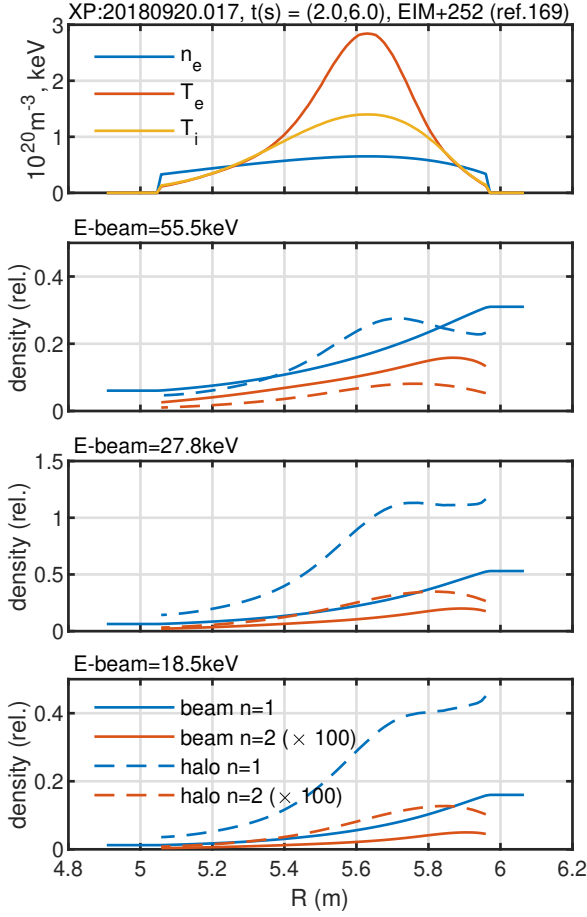
Figure 4. Plasma parameters along the neutral beam (top). Relative densities of beam and halo neutrals in ground ($n = 1$) and first excited ($n = 2$) states. The $n = 2$ densities are multiplied by 100 for visualization. The second to fourth plots correspond to the first, second and third beam energy components, with initial fractions equal to (31%, 53%, 16%). The neutral beam is injected from the right side of the plots and attenuates as it propagates towards smaller R values (see figures 1 and 2 of [16])). Note that, in these plots, the halo densities are formally divided in three parts, depending on the energy component they originated from. The total hallo density is then given by the sum of the three parts.

derived from the charge exchange cross sections (figure 3) allows to determine the relative contribution to the measured signal of the several $C^{6+} + H^0$ charge transfer processes. The signal composition, in turn, enters the evaluation of the cross-section corrections to the velocities that are presented in Appendix B. Figure 6 shows an example of the CXRS signal composition and velocity corrections for one of the discharges that will be presented later in figures 7 and 10. It can be seen that the velocity corrections are a significant fraction of the measured values and that the halo density must be considered since it contributes a large fraction to the CXRS signal at the plasma core.
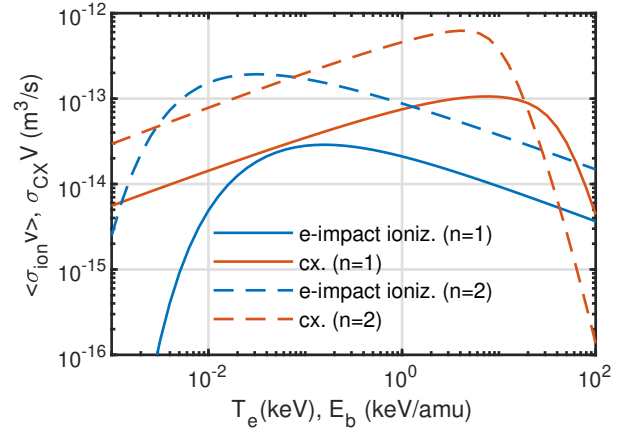
3. Inverted flows and comparison with neoclassical expectations

The CXRS system at W7-X provides several (~ 50) C^{6+} velocity measurements along the path of a radial neutral beam heating line. Each view line determines the projection of the local velocity measurement and belong to either the toroidal, $+45°$ or $-45°$ arrays. The naming refers to the approximate direction of the view lines with respect to the local magnetic field. We refer the interested reader to [16] for a description of the instrument and viewing geometry. To avoid overburdening the text, we defer most information on the inversion method to the appendices. Therein we provide detailed descriptions of how the multiple velocity measurements are corrected (Appendix B), interpreted and combined (Appendix A) to find the radial profiles of radial electric field, $E_r(\rho)$, and net carbon parallel velocity, $V_\parallel(\rho)$, that best reproduce the measurements. The variable ρ is a normalised radial coordinate defined in Appendix A. The essential steps of the inversion method are:

(i) Using the neutral beam model described in section 2 (see figure 4), calculate the CXRS signal composition (see figure 6 centre).

(ii) Compute the velocity corrections given by (B.1) and by equation (B.11) with the known beam parameters and CXRS signal composition.

(iii) Using the flow geometry described in Appendix A, construct a forward model for the individual velocity measurements for given parametrised E_r and $V_\parallel$ profiles.

(iv) Iterate on E_r and $V_\parallel$ profile parameters to minimise an error function that quantifies the
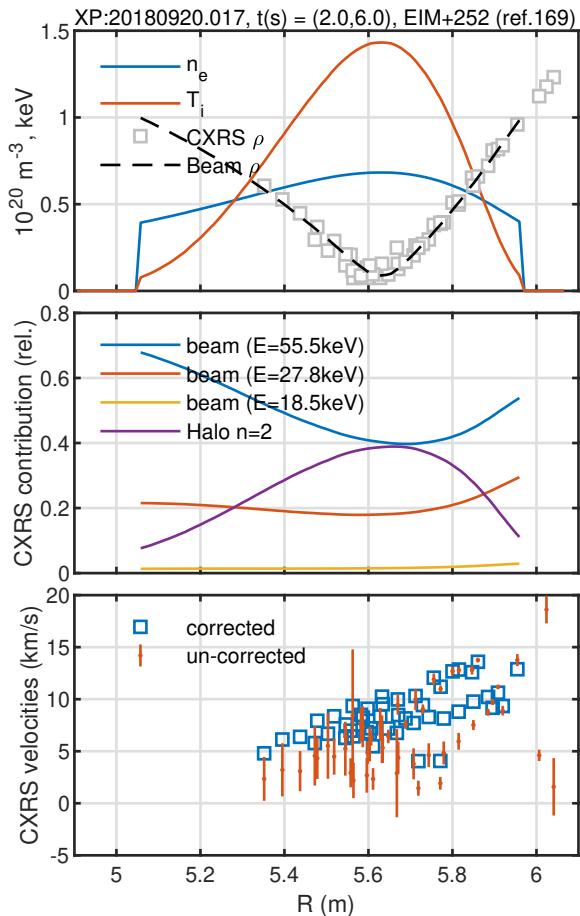
Figure 6. Top: beam parameters and radial position (black dashed line) and location of the CXRS measurements (empty squares). Middle: relative contributions to the CXRS signal of the three neutral beam energy components (ground state) and the n=2 population of the beam halo. The relative contribution of the $n = 2$ beam populations is small (less than a few percent) and not shown in this plot. Bottom: corrections of the measured velocities due to fine structure, cross section and finite lifetime (see Appendix B).

difference between the forward-modelled velocities and those resulting from (ii).

We note that the flow model referred to in (iii) relies on two assumptions: (1) the perpendicular flow is of $E \times B$-type, i.e. $\mathbf{V}_\perp \sim \nabla\psi \times \mathbf{B}/B^2$ (see notation in Appendix A) and (2) the total flow is incompressible $\nabla \cdot \mathbf{V} = 0$. Any variation of the velocity measurement due to magnetic geometry (i.e. flux compression, local B-field direction, ratio of parallel Pfirsch-Schlüter to perpendicular flow, etc.) is accounted for by the projections of the relevant vectors on the viewing direction and decoupled from the variation of the flow-defining radial functions, $E_r(\rho)$ and $V_\parallel(\rho)$.

In the remainder of this section, this method is used on CXRS data obtained for different plasma conditions and the resulting profiles are compared with neoclassical calculations. The shots analysed

are heated by electron cyclotron resonance heating (ECRH) with short (10 or 20 ms) NBI blips for enabling and accurate determination of the active CXRS spectroscopic component. The neoclassical calculations were done with the DKES [35] code and validated with SFINCS [28] runs, that employs the full linearised Fokker-Planck collision operator, at a reduced set of radial locations. In both cases, electrons, hydrogen ions and fully stripped C^{6+} impurity were included. Differences between the SFINCS and the DKES simulations, which use a simplified collision operator, were found to be small, so only DKES profiles will be presented and discussed in this section. For the calculation of $V_\parallel$ from the DKES coefficients, the Taguchi implementation of momentum correction [38, 29] was used. We note that the inclusion of momentum correction in the neoclassical modelling is quantitatively important for the paralllel velocities.

3.1. Density scan at constant power in the standard magnetic configurations

First we study the inverted flows for three stationary discharges with different densities (figure 7), but otherwise similarly heated with 4.7 MW of X2-ECRH. Since the density increase enhances the electron-to-ion heat transfer, the temperature of the electrons is reduced more strongly than that of the ions. As a result, the neoclassical core electron root ($E_r > 0$) feature of these plasmas is expected to be reduced for increasing density and therefore provide a suitable set for comparison. The parallel main ion velocity shown in the lower plots of figure 7 is small and negative, as expected from the low mirror term of the standard magnetic configuration (EIM) used in these plasmas.

The CXRS inverted flows for each of the three discharges are compared to these calculations in figures 8, 9 and 10. To reduce statistical errors, the CXRS measurements are averaged over 4 seconds with stationary plasma parameters. The upper plots in these figures show the flow-defining profiles (namely the radial electric field, E_r, and net parallel C^{6+} rotation, $V_\parallel$, whose definition can be found in (A.13)) that result from the inversion process as well as from neoclassical calculations. The lower plots show the actual velocity measurements compared to those forward-modelled from the experimental (blue points) and neoclassical (yellow crosses) profiles in the upper plots. The experimental E_r and $V_\parallel$ are in fact determined in the inversion process by minimising the distance between the forward-modelled velocities and the measurements (see Appendix A.2).

Several aspects of this comparison are to be highlighted: first and foremost, an overall agreement with neoclassical expectations in flow sign and broadly speaking similar magnitudes are found for the three
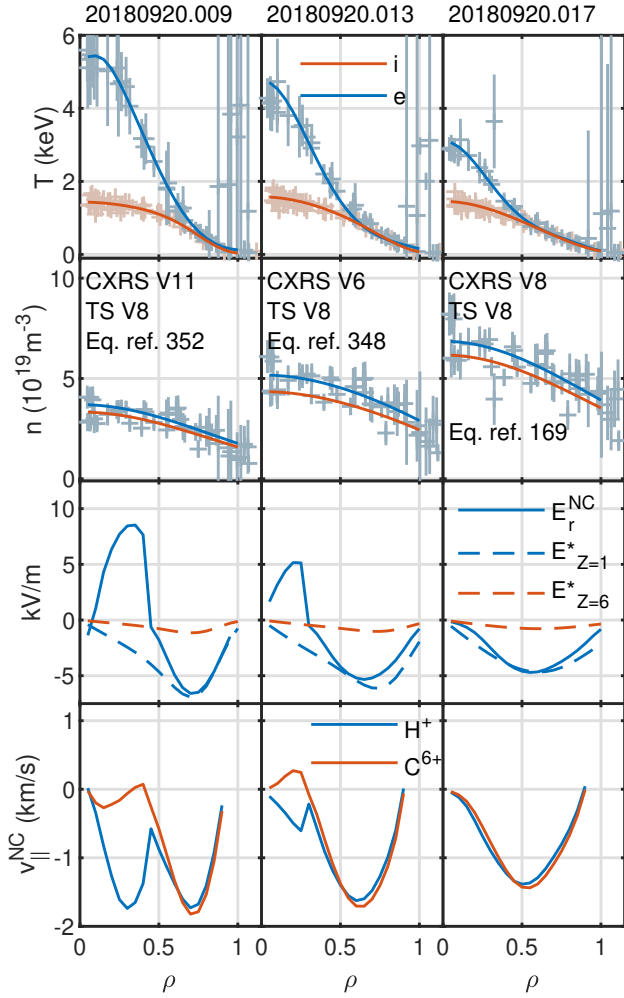
Figure 7. Experimental and calculated profiles for three shots with increasing density from the sequence 20180920 in standard configuration EIM+252. Reference numbers indicate the magnetic equilibrium used for the diagnostic mapping. First and second rows: experimental temperature and density profiles (data points and fits) from the Thomson scattering (TS) and CXRS systems. The experimental profiles are averaged over the time interval [2.0, 6.0]s. Ion density is calculated assuming a constant $Z_{\rm eff} = 1.5$ and C^{6+} as only impurity. Third and fourth rows: neoclassical ambipolar radial electric field and net parallel velocity of main ions (H^+) and C^{6+} calculated with the DKES code. Also plotted are the equivalent diamagnetic electric fields $E_Z^* = (dp_Z/dr)/Zen_Z$, for main ions and the C^{6+} impurity under the assumption of constant concentration.

shots. This is also the case for the other shots discussed later in this section. Furthermore, the expected reduction of the central electron root ($E_r > 0$) for increasing plasma density is clearly captured by the measurements. The central values of both E_r and $V_\parallel$ are generally compatible with zero or very low velocities, as one would expect from the gradient drive in the drift-kinetic description of first order flows. Second, the compatibility of the flow model with the (at some positions redundant) velocity measurements
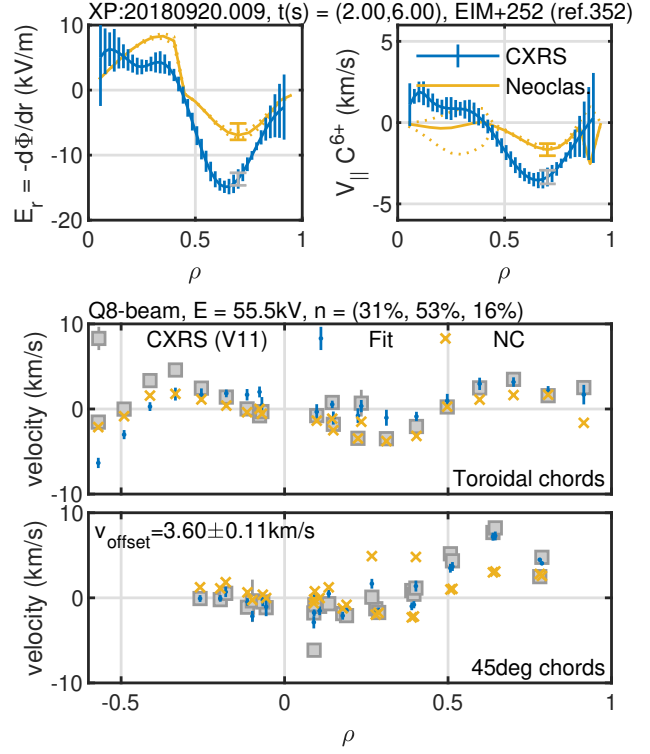

Figure 8. Top: Inverted radial electric field and net parallel rotation profiles from CXRS data averaged over seven 20 ms long NBI blips during a 4 s long stable phase of the discharge 20180920.009. The yellow lines correspond to neoclassical DKES calculations for the profiles shown in 7. The dotted line shows the variation associated to a $Z_{\rm eff} = 1.5 \pm 0.3$, whereas the error bar at $\rho = 0.7$ show the variation due to a $\pm 20\%$ variation of the local radial gradients of n, T_e and T_i. Blue error bars reflect the uncertainty in the minimisation procedure and the gray error bar shows the typical error due to the fitting of the spectral line. Bottom: comparison of the CXRS measured velocities to those forward-modelled from the profiles shown in the top figure. A global velocity offset due to the instrumental spectral drift is also obtained from the minimisation procedure. The beam identifier, primary energy of the beam and the beam composition used for the cross-section corrections are shown above the middle plot.

is found to be good except for some toroidal chords in the high field side of the neutral beam path (negative ρ values in the velocity plots of figures 8 through 10)§

In spite of the qualitative agreement, the comparisons in figures 8, 9 and 10 show clear deviations of the measurements with respect to the neoclassical calculations beyond the measurement and inversion error bars, both in the radial electric field and net parallel rotation. These differences appear most evident around $\rho = 0.6$ where the inverted E_r and $V_\parallel$ can be twice larger than the neoclassical expectations. While the differences in velocities are

§ This type of deviations has been interpreted in previous works as an evidence of in-surface density variations of C^{6+} ([see e.g. 30, 34, 1, and references therein]). Further analysis and better statistics will be required to confirm whether this is a likely explanation of the observations at W7-X.
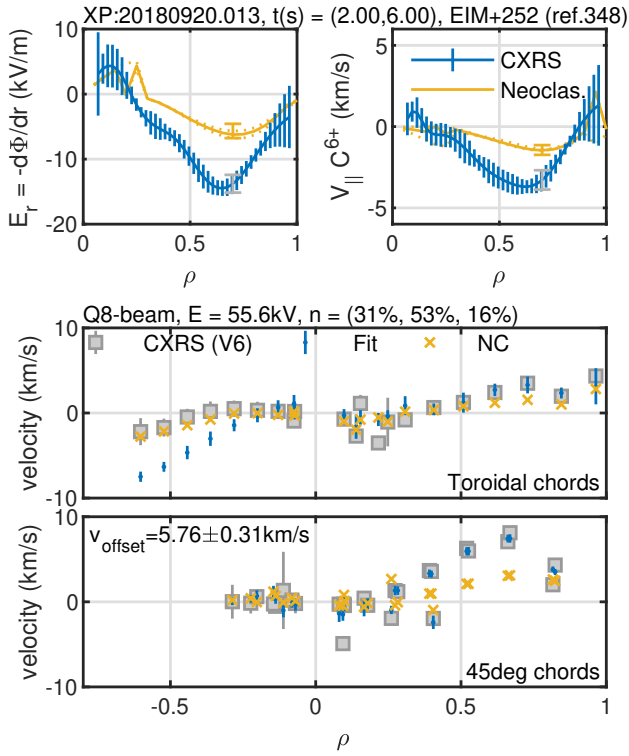
Figure 9. Inverted E_r and $V_\parallel$ profiles compared with neoclassical calculation for discharge 20180920.013. Details as in figure 8.
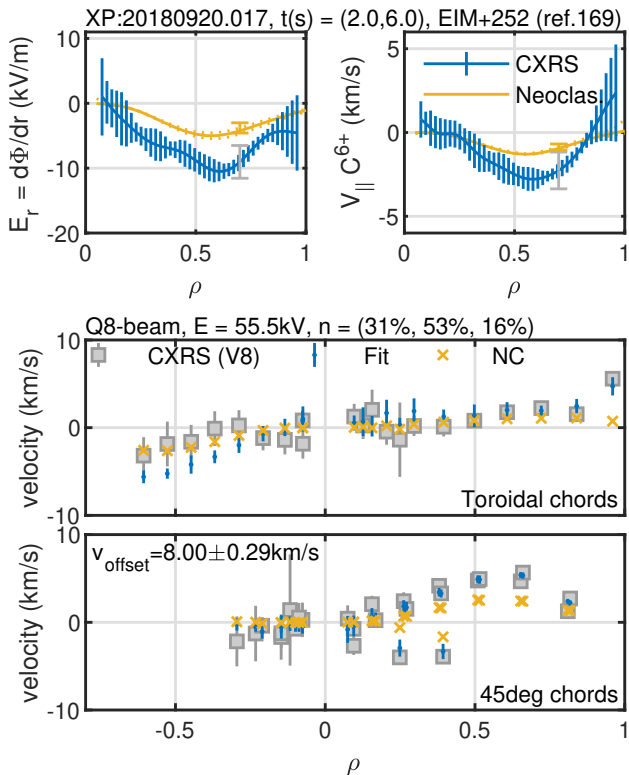

Figure 10. Inverted E_r and $V_\parallel$ profiles compared with neoclassical calculation for discharge 20180920.017. Details as in figure 8.

small by spectroscopic standards (in the range of few km/s), they are larger than the estimated error bars‖.

3.2. Density step at constant power in the high-mirror magnetic configuration

The mirror term is a key element in the neoclassical optimization of W7-X: within the configuration space of W7-X, the higher toroidal mirror term is known to cause increased effective ripple and reduced bootstrap transport coefficients [5, 17]. For similar profiles, the increased effective ripple is expected to affect the radial electric field, via a larger contribution of the electrons to the ambipolar equation, see e.g. [40]. In plasmas transiting from electron to ion root, the region of positive E_r should be wider; additionally, E_r should become more positive in electron root and less negative in ion root. With respect to the ion parallel flow, the relative reduction of the bootstrap current coefficient should translate into a reduction of the ion flow¶.

To investigate some of these aspects we now turn our analysis to plasmas produced in the high mirror magnetic configuration. Figure 11 shows the plasma profiles averaged over two stationary time intervals in this configuration. The corresponding calculated neoclassical flows are shown in the same figure. The ECRH power is approximately the same (4.7 and 5.3 MW), but plasma density is higher in the second interval. Note that the kinetic profiles for these two intervals are comparable to those of discharges 13 and 17 in figure 7.

The respective inversions are shown in figures 12 and 13. The inverted E_r and $V_\parallel$ compare well with the neoclassical estimates and, as in the previous inversions, capture the transition from electron to ion root in the central portion of the plasma. Overall, the agreement with the calculated neoclassical flows is better than for the standard configuration (figures 8 to 10). The higher toroidal mirror term, b_{01}, of the high-mirror configuration results in a larger effective ripple and a stronger damping of the net parallel flow of the main ion and the C^{6+} impurity (cf. 7 and 11). It is noteworthy that this tendency is reflected in the experimental $V_\parallel$ (cf. figs. 10 and 13). This observation supports those reported in [14] where the effect of the mirror term on the parallel bootstrap current was demonstrated.

‖ It should be noted that errors due to the uncertainties in the beam model used for the calculation of cross sections effects (see Appendix B) are not accounted for. Similarly, misalignment of the optical fibres of up to 0.03 in rho is possible, but not considered in the present error analysis

¶ Note that, in ion-root conditions, ions contribute a relatively small fraction of the total bootstrap current compared with electrons.
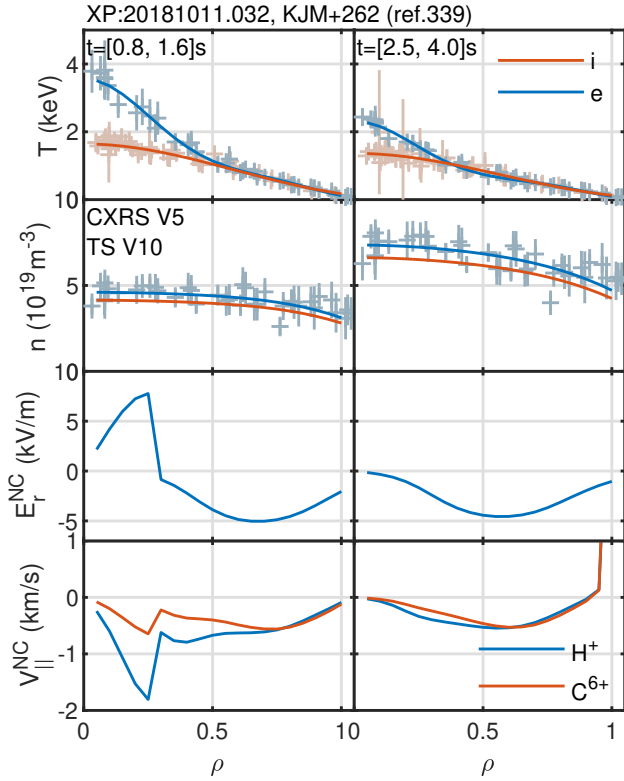
Figure 11. Experimental and calculated profiles averaged over two time intervals in the discharge 20181011.032 in the high mirror magnetic configuration. The ECRH heating power was 4.7 and 5.3 MW in the two respective intervals. Reference numbers indicate the magnetic equilibrium used for the diagnostic mapping. First and second rows: experimental temperature and density profiles (data points and fits) from the Thomson scattering (TS) and CXRS systems. Ion density is calculated assuming a constant $Z_{\text{eff}} = 1.5$ and C^{6+} as only impurity. Third and fourth rows: neoclassical ambipolar radial electric field and net parallel velocity of main ions (H^+) and C^{6+} calculated with the DKES code.

3.3. Flow profile evolution during the high-performance post-pellet phase

The plasmas with maximum performance in the OP1.2 experimental campaign were observed after series of pellets injections followed by a decay of the plasma density and a rapid increase of ion temperature. The diamagnetic energy increases alongside the temperatures reaching record values above 1 MJ, i.e. an average plasma $\beta \sim 1\%$ [9, 3]. In [6] a high-performance shot was used to demonstrate the successful reduction of neoclassical heat transport in the W7-X configuration.

Figure 14 shows the evolution of several plasma parameters during such a discharge, analysed in detail in [9]. Time traces of the values of E_r and net parallel velocity for several radial positions are shown in the lower two axis. During the increase of the diamagnetic energy (W_{dia}) a pronounced increase
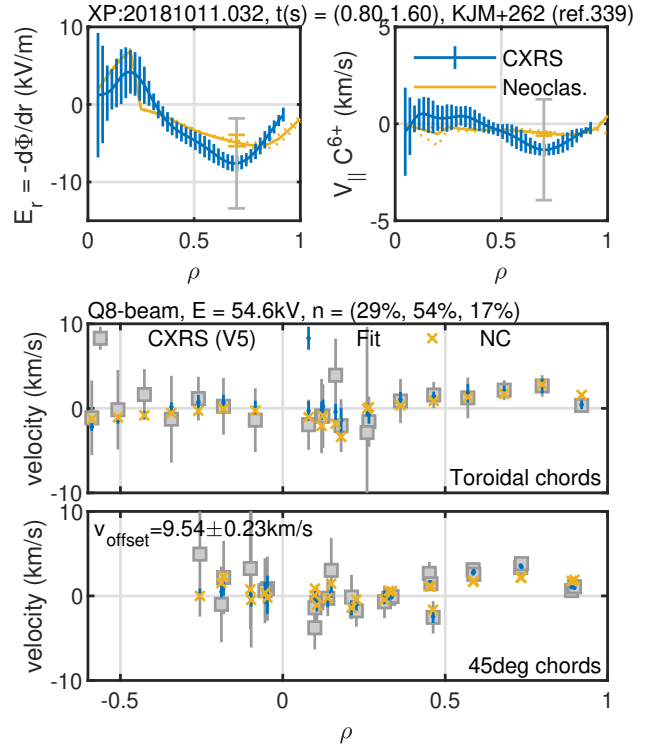

Figure 12. Inverted E_r and $V_\|$ profiles compared with neoclassical calculation for discharge 20181011.032. Details as in figure 8.

of the magnitude of the negative E_r and $V_\|$ is observed around $\rho = 0.6$. A similar evolution of the radial electric field has been recently reported with Doppler reflectometer measurements in high-performance discharges [15]. Here we show for the first time that, based on the analysis of CXRS data, the ion net parallel velocity appears to experience a similar increase as the energy content of the plasma rises, reaching values above 10 km/s in the direction opposite to the magnetic field. While the calculated parallel neoclassical flow does increase as well, it falls short of the measurements by a considerable factor in the region where the measurements display a strongest dip. We note that, as already reported in [6], the agreement between the neoclassical and the inverted radial electric field profiles is reasonably good in the high-performance phases (see Extended Data Fig.3 in that reference). The confirmation of this strong parallel flow in high performance discharges as well as its possible involvement in the evolution and termination of the high performance phase will be the subject of future investigations, which is only possible at W7X using CXRS measurements and the analysis presented here.
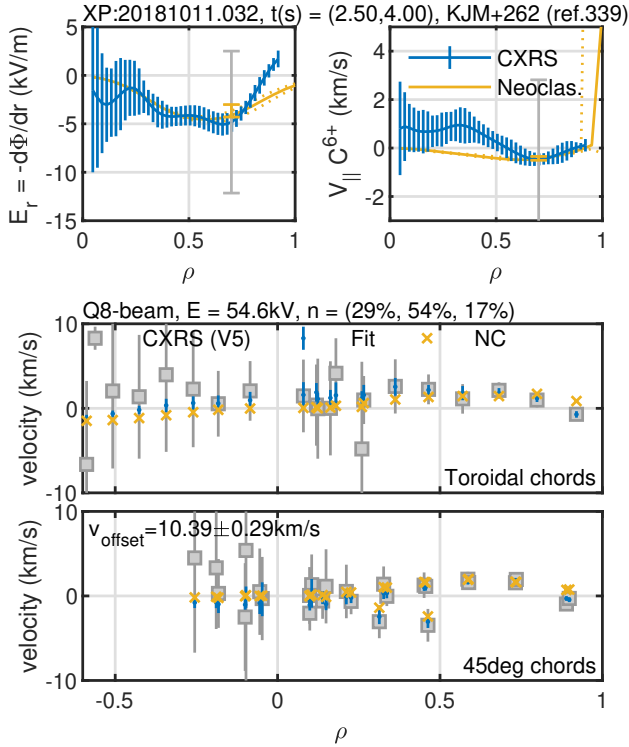
Figure 13. Inverted E_r and $V_\parallel$ profiles compared with neoclassical calculation for discharge 20181011.032. Details as in figure 8. Note that the offset velocity that is determined in the minimisation loop is about 1 km/s larger than the one found for an earlier time interval in the same discharge (see figure 12). Wavelength shifts due to thermal drifts of the spectrometer are not expected to vary within the duration of a discharge, so this difference gives a measure of the accuracy in the determination of the offset velocity.
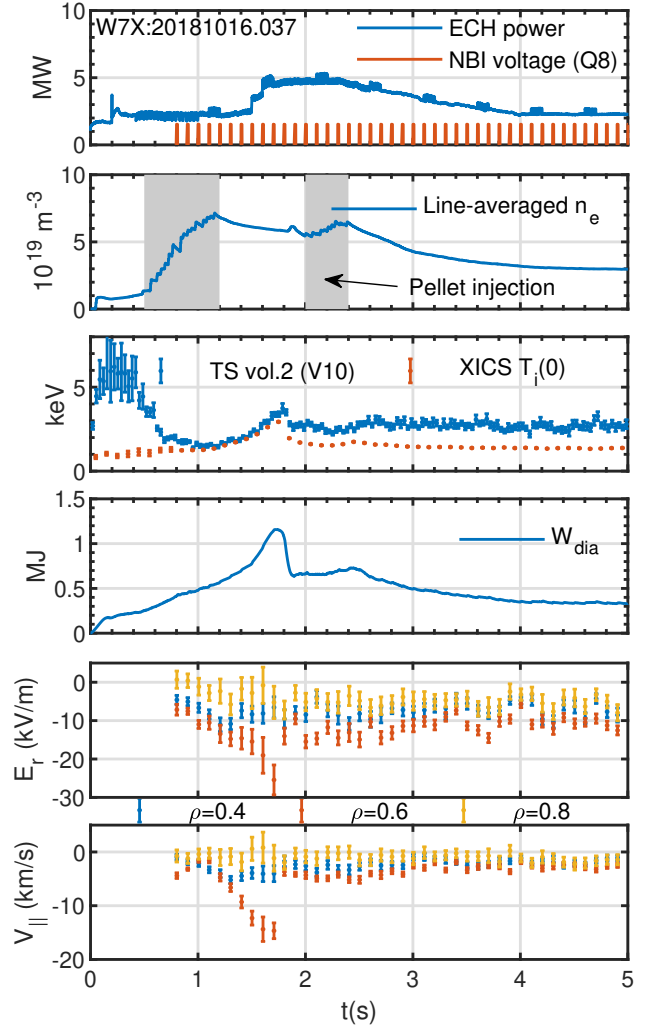

Figure 14. Plasma parameter evolution in a high performance pellet discharge. From top to bottom: ECRH power and NBI blips, line-averaged electron density, central ion (XICS) and electron (Thomson Scattering) temperatures, diamagnetic energy, CXRS radial electric field and net C^{6+} parallel velocity at $\rho = 0.4, 0.6$ and 0.8. Two trains of pellets were injected during the time intervals $[0.5, 1.2]$ s and $[2.0, 2.4]$ s. Only the first of them was successful in causing a subsequent high-performance phase.

4. Discussion

In the previous section we presented cases for which the radial electric field and net parallel velocity measured with CXRS displayed differences with respect to the neoclassical flows. In Wendelstein 7-X, several diagnostic techniques allow to measure the radial electric field independently. Figure 16 shows a comparison of the CXRS E_r with the one measured by means of Doppler Reflectometry (two measurements in the V and W band are shown) and the X-Ray Imaging Crystal Spectrometer (XICS) for the three shots and times shown in figures 8, 9 and 10. Whereas the various measurements overlap within error bars at particular points, there are obvious disagreements for others. This suggests that more work may be required in identifying and correcting small systematic errors in the analysis of one or more of them. Until this is done, it not reasonable to claim any systematic departure of the experimental E_r with respect to neoclassical calculations.

Furthermore, the cross-diagnostic E_r comparison

shown in figure 16 shows that CXRS tends to give values that are more negative than both the neoclassical ambipolar E_r and other diagnostic measurements. Although particular instances can show a better agreement (see figures 12 and 13), this observation begs the question whether the implementation of the CXRS technique or the interpretation of its data might be affected by diagnostic-specific issues. In this respect, one should note that the corrections of the radial electric field due to the diamagnetic velocity of the C^{6+} ions is expected to be smaller than the experimental errors. This was illustrated in figure 7 (dashed red line) under
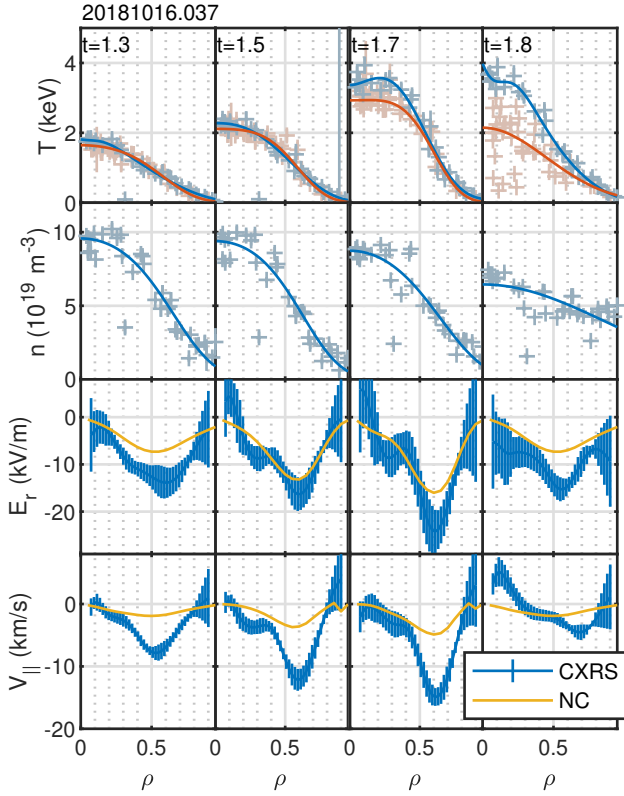
Figure 15. Profile evolution during the build up phase of high performance (W_{dia}) immediately after the injection of hydrogen pellets ($\sim$1.2 s) in the high performance discharge shown in figure 14. We note that there are fitting artefacts in the electron temperature central profile for t =1.7 and 1.8 s which do not affect the discussion.

the assumption of approximately constant carbon concentration (see [16]). The so-called *active* charge exchange spectra is acquired during NBI blips of 10 or 20 ms duration. Being localised in that phase, one can conceive that the neutral beam itself could be affecting the radial electric field. Next we examine several potential effects related to beam-induced changes in the ambipolar fluxes. However, we observe that none of them seems capable to produce the observed departures in the radial electric field.

Radial current due to NBI-produced fast ions. Since the CXRS measurements are performed on the NBI blips, it is legitimate to ask whether they can alter the radial current balance and the resulting electric field. The blips do not significantly affect the plasma main parameters so one would not expect changes in the radial electric field due to profile modification in the short NBI injections. Furthermore, the radial current due to the fast ions produced by the NBI is too small compared to neoclassical currents to measurably affect the ambipolar radial electric field. This is supported by ASCOT simulations shown in figure 17. The predicted

fast ion flux of about 3×10^{19} s^{-1} at the radial position $\rho = 0.6$ produces a radial current density of about 6×10^{-2} A/m^2. Referring now back to figure 2, it is clear that such a current density would only very slightly modify the neclassical ambipolar E_r.

Radial current induced by NBI-produced neutral atoms. Another potential effect on plasma flows related to the beam injection is that of the friction exerted by the halo and beam neutrals on the main ions through charge transfer reactions. From the momentum balance equation one can show that the size of the related radial current density is given by

$$\langle \mathbf{j} \cdot \nabla r \rangle \sim Z_i e (\rho_i^*)^2 a n_i n_0 A_b \langle \sigma_{CX} v \rangle \ , \tag{4}$$

where ρ_i^* is the normalised ion gyroradius, a is the minor radius, n_i and n_0 are the ion and beam neutral densities and A_b is the ratio of the beam section (of radius $\sim$ 15 cm) to the flux surface area ($\sim$ 100 m^2). A typical number for this ratio is $A_b \sim 10^{-3}$. Typical numbers for ion temperature $T_i \sim 1$ keV and density $n_i \sim 5 \times 10^{19}$m^{-3} yields

$$\langle \mathbf{j} \cdot \nabla r \rangle \sim 5.31 \times 10^{-5} [\mathrm{sA/m^2}] \times n_0 A_b \langle \sigma_{CX} v \rangle \ , \tag{5}$$

The neutral density along the beam can be estimated from the total beam power (1.5MW) and the relative densities and velocities at the plasma entrance shown in figure 4 to give $n_0 \sim 5 \times 10^{15}$m^{-3}. Together with the typical reaction rates (see figure 5), the current due to the CX friction between beam neutrals and plasma ions is estimated to be in the 10^{-5} A/m^2 range, which is a negligible modification of the neoclassical current balance. Typical densities for recycling neutrals in the edge are also $n_0 \lesssim 10^{15}$m^{-3} averaged over the plasma edge. The current density due to these edge neutrals is therefore about 10^2-10^3 times larger than the one estimated for NBI neutrals, but is still irrelevant in determining the ambipolar E_r.

To finalise this section, we briefly discuss two instrumental issues of importance for the determination of the CXRS velocities. Namely, the determination of the passive emission and the wavelength calibration.

Contamination by passive emission. The correct separation of the active and passive emission is critical to flow measurements, particularly for core measurements where the active component velocity is significantly different to the passive contribution originating from the edge. The measurements presented in this work are taken from fits to spectra after subtracting the average signals from before and after short 10-20 ms NBI blips and this subtraction method works well for Doppler broadening T_i measurements up to 30 ms blips [16]. The Doppler shift is significantly more sensitive to small deformations to the spectra and small changes to
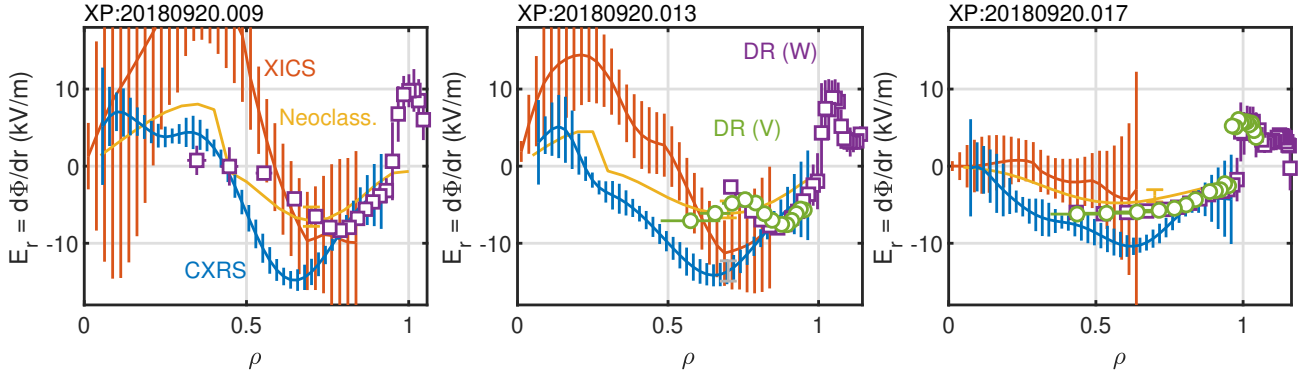
Figure 16. Comparison of radial electric field profiles from several diagnostics (XICS, Doppler Reflectometry in the W and V bands and CXRS) and the three plasma discharges analysed before. The yellow line corresponds to the neoclassical ambipolar radial electric field.
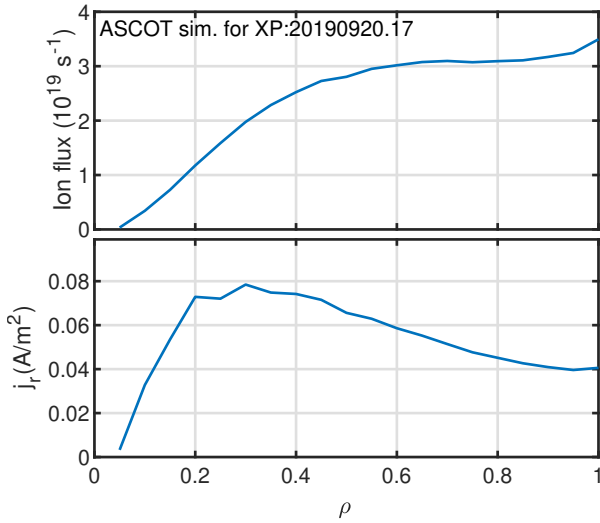

Figure 17. Fast ion integrated flux and current density as calculated by ASCOT for the profiles and beam parameters of discharge 20190920.017 (see figure 7).

the passive component within 20 ms might play a role, particularly on the in-board side measurements ($\rho < 0$) where the active component is weak due to beam attenuation. It is however not expected that a significant distortion would be produced at $\rho \sim 0.6$, where the strongest deviation from neoclassical predictions are seen. Nevertheless, the passive/active separation will be significantly improved in the next experimental campaign in order to rule out this possibility.

Wavelength calibration. The small velocities measured require a wavelength calibration precise to at least 1/10 of a pixel in the spectrometer, which is conducted for all spatial channels before and after the experimental campaign. While the wavelength is observed to drift during tests on an hour timescale, this was consistent for all spatial channels and so is ac-

counted for by the single free parameter in the fitting process. The value is effectively constrained by consistency of the +45° and -45° observations. If an additional drift with dependence on the spatial channel were present, it could in principle lead to the deviations observed. In order to remove this possibility as well as the need for the free parameter, future measurements will include a wavelength calibration on a small number of channels directly before and after each plasma discharge.

5. Conclusion

We have presented inversions of the radial electric field and net parallel rotation of the C^{6+} ions from the measurements of the multi-chord CXRS system in W7-X. Detailed treatments of the 3D flow, the viewing geometry and the atomic physics corrections were implemented. The inverted E_r and $V_\parallel$ profiles show an overall consistency with neoclassical expectations in size, sign and tendency with the plasma conditions and magnetic geometry. Nevertheless, quantitative differences of 1 to 10 km/s are often observed around mid-radius. Compared to the neoclassical values, the inverted flows can be twice as large at those locations. For the case of E_r, the comparison with other diagnostics does not support the existence of an experimental deviation from the neoclassical ambipolar E_r. The causes of the suspected flow overestimation in the analysis and interpretation of CXRS measurements will be the subject of future investigations with the calibration improvements outlined in section 4 as well as a larger dataset, additional spectrometers and extending the analysis to impurities other than C^{6+}. As a particular case of discrepancy, high performance phases display a remarkably increased parallel flow with the direction and shape predicted by neoclassical calculations, but otherwise clearly in excess of it. In as much as the understanding and control of transport

reduction in W7-X high performance discharges is important to extend the device operational range, this observation merits further investigation.

Appendix A. Description of the flow geometry, conventions and definitions

We assume that the first order flow field of the C^{6+} impurity species is incompressible. The order here refers to the scaling with the normalised gyroradius. Since radial flows are second order in this parameter, the leading-order flow is tangent to the flux surfaces. We can then write the flow field as

$$\mathbf{V} = \omega(\psi)\left(\frac{\nabla\psi \times \mathbf{B}}{B^2} + \frac{h}{B}\mathbf{B}\right) + \frac{\langle \mathbf{V} \cdot \mathbf{B}\rangle}{\langle B^2\rangle}\mathbf{B} \ , \qquad (A.1)$$

where $\mathbf{B}$ is the magnetic field. The function h accounts for the Pfirsch-Schlüter parallel flow and is defined by

$$\nabla \cdot \left(\frac{\nabla\psi \times \mathbf{B}}{B^2} + \frac{h}{B}\mathbf{B}\right) = 0 \ , \qquad (A.2)$$

and $\langle hB\rangle = 0$. The radial variable ψ is chosen to be the proportional to the torodial magnetic flux Ψ_T, $2\pi\psi = \Psi_T$ and the resulting angular frequency ω is given by the sum of the $E \times B$ and diamagnetic perpendicular flows

$$\omega(\psi) = -\frac{d\Phi}{d\psi} - \frac{1}{n_s Z_s e}\frac{dp_s}{d\psi} \ . \qquad (A.3)$$

We will work in Boozer coordinates, with Jacobian $\sqrt{g} = \frac{V'(\psi)}{4\pi^2}\frac{\langle B^2\rangle}{B^2}$ and co- and contra-variant expressions of the magnetic field given by:

$$\mathbf{B} = I(\psi)\nabla\phi + J(\psi)\nabla\theta + \eta\nabla\psi \ , \qquad (A.4)$$

$$\mathbf{B} = \frac{1}{\sqrt{g}}\left(\iota \mathbf{e}_\theta + \mathbf{e}_\phi\right) \ , \qquad (A.5)$$

where I and J are proportional to the poloidal and toroidal current respectively.

Taking $\sqrt{g}\nabla\psi\times$ of equation (A.4) and using $\sqrt{g}B^2 = I + \iota J$ one gets

$$\frac{\nabla\psi \times \mathbf{B}}{B^2} = \left(\frac{J}{I + \iota J}\right)\mathbf{e}_\phi - \left(\frac{I}{I + \iota J}\right)\mathbf{e}_\theta \ . \qquad (A.6)$$

The expressions above relate the co-variant base vectors $\mathbf{e}_\theta$ and $\mathbf{e}_\phi$ to the geometric vector field that define the flow in equation (A.1). To calculate them we will make use of their relation to the angular derivatives of the cylindrical coordinates (R, z, φ) which are provided as a function of (θ, ϕ) in the equilibrium. Namely,

$$\begin{aligned}\mathbf{e}_\theta &= \frac{\partial\mathbf{r}}{\partial\theta} = \frac{\partial R}{\partial\theta}\frac{\partial\mathbf{r}}{\partial R} + \frac{\partial z}{\partial\theta}\frac{\partial\mathbf{r}}{\partial z} + \frac{\partial\varphi}{\partial\theta}\frac{\partial\mathbf{r}}{\partial\varphi} \\ &= \frac{\partial R}{\partial\theta}\hat{\mathbf{R}} + \frac{\partial z}{\partial\theta}\hat{\mathbf{z}} + R\frac{\partial\varphi}{\partial\theta}\hat{\boldsymbol{\varphi}}\end{aligned} \qquad (A.7)$$

Using equations (A.4) and (A.5), the magnetic differential equation (A.2) for h/B reads

$$(\iota\partial_\theta + \partial_\phi)\frac{h}{B} = -(J\partial_\phi - I\partial_\theta)\left(\frac{1}{B^2}\right) \ , \qquad (A.8)$$

which can be solved algebraically after Fourier transforming. We note that the solution of this equation can have large resonant components close to rational surfaces. Those flux surfaces (which, for the magnetic configurations considered in this work, lie in the neighbourhood of $\iota = 10/11$ close to $\rho = 0.73$) are removed from the matrix of geometric coefficients used for 3D interpolation.

Note on left-handed basis and B-field direction. The expressions derived here are valid for a right-handed coordinate system and magnetic field with a positive toroidal component $B^\phi > 0$. The Jacobian $\sqrt{g}$ is assumed positive. However, the VMEC coordinate system and the Boozer coordinates derived from those are left handed: the poloidal angle θ grows in the counter-clockwise direction when viewed in the direction (counter-clockwise as seen from the top) in which the toroidal angle ϕ grows. This causes some sign changes in the relation of the covariant and contravariant basis vectors. To account for this fact, the RHS of equations (A.6) and (A.8) have to be multiplied by (-1). Equation (A.4) assumes that B^ϕ is positive, which is the case for the normal field direction in W7-X. If this is not the case, the RHS of (A.4) and (A.8) need to be multiplied by (-1).

Appendix A.1. Normalization and geometric objects

For dimensional convenience, we will re-write equation (A.1) and define the vectors that will be computed for forward-modelling of the ion flow. We define a flux surface minor radius r as

$$r = a\sqrt{\frac{\psi}{\psi_a}} \ , \qquad (A.9)$$

where a is the minor radius and ψ_a the value of ψ at the last closed magnetic surface. The normalised radius ρ is defined as $\rho = r/a$. We define a constant

that characterises the typical size of the magnetic field as

$$B_0 = \frac{2\psi_a}{a^2} . \quad (A.10)$$

With these definitions,

$$\frac{d\Phi}{d\psi} = \frac{a^2}{2r\psi_a}\frac{d\Phi}{dr} = \frac{1}{rB_0}\frac{d\Phi}{dr} \quad (A.11)$$

and the flow expression (A.1) can be rewritten as

$$\mathbf{V} = (V_E + V_{dia,s})\frac{1}{r}\left(\frac{\nabla\psi \times \mathbf{B}}{B^2} + \frac{h}{B}\mathbf{B}\right) + V_\parallel \frac{\mathbf{B}}{B_0} , \quad (A.12)$$

where the several velocities are defined as

$$V_E = \frac{-1}{B_0}\frac{d\Phi}{dr} = \frac{E_r}{B_0} ,$$
$$V_{dia,s} = \frac{-1}{Z_s e n_s B_0}\frac{dp_s}{dr} , \quad (A.13)$$
$$V_\parallel = \frac{\langle \mathbf{V} \cdot \mathbf{B}\rangle B_0}{\langle B^2\rangle} .$$

In fitting the CXRS flow measurements at different points, we will evaluate the dimensionless vectors

$$\boldsymbol{\mu} = \frac{1}{r}\left(\frac{\nabla\psi \times \mathbf{B}}{B^2} + \frac{h}{B}\mathbf{B}\right) \quad (A.14)$$

and

$$\boldsymbol{\lambda} = \frac{\mathbf{B}}{B_0} \quad (A.15)$$

at each of those points. We note that these vectors are invariant under constant scaling of the equilibrium $\mathbf{B} \to \alpha\mathbf{B}$. The only influence of the overall field strength is the relation of the velocities (A.13) to other physical quantities such as E_r.

Appendix A.2. Inversion procedure

The goal of the flow inversion procedure described here is to find the profiles of $(V_E + V_{dia,s})(r)$ and $V_\parallel(r)$ that best fit the set of velocity measurements in different positions along the neutral beam. In order to do this we will adopt a forward-model approach. Starting from an initial parametric representation of the profiles, we forward-model the velocities at each of the measurement point $\mathbf{r}_i$ in the direction $\mathbf{u}_i$,

$$V_i^{\text{fw}} = \mathbf{V}(\mathbf{r}_i) \cdot \mathbf{u}_i =$$
$$(V_E(\rho_i) + V_{dia,s}(\rho_i))\boldsymbol{\mu}(\mathbf{r}_i)\cdot\mathbf{u}_i + V_\parallel(\rho_i)\boldsymbol{\lambda}(\mathbf{r}_i)\cdot\mathbf{u}_i . \quad (A.16)$$

The projections $\boldsymbol{\mu}\cdot\mathbf{u}_i$ and $\boldsymbol{\lambda}\cdot\mathbf{u}_i$ for the different CXRS lines of sight are shown in figure A1.

Next we iterate the parametric representation of the flow profiles to find a local minimum of the mean squared deviation $\sum_i W_i(V_i - V_i^{\text{fw}})^2$. The contribution of each measurement to the error function is weighted by a factor W_i, that accounts for the measurement error, to reduce the influence of large-error data points in the Nelder-Mead minimisation algorithm.

The overall velocity offset that results from slow (inter-shot) thermal drifts in the spectrometer is also determined in the minimisation procedure (a factor added to equation (A.16), equal for all data points). To determine the error in the inverted profiles, the minimisation is repeated 100 times with randomised initial conditions. For the parametric representation of the velocity profiles we choose the sum of ten radially shifted Gaussians. Other parametrisations (e.g. a tenth degree polynomial) produce similar results. We note that the form used in this work does not require the perpendicular velocity to be zero at the centre, yet the inversions are consistent with this expectation.

Appendix B. Atomic physics corrections of the observed CXRS velocities

Appendix B.1. Fine-structure correction

Analytical simulations of line shapes from quantum transitions in hydrogen-like atoms including fine-structure and Zeeman splitting were carried out by Blom and Jupén for fusion-relevant temperatures [8]. In that reference it was shown that the central wavelength of a gaussian fit to the unresolved $n = 8 \to 7$ transition line of hydrogen-like carbon experiences a shift that depends on the real ion temperature and is independent of the magnetic field strength and orientation (see figure 8 in [8]). In the present study we use the following approximation to the rest wavelength

$$\lambda_0(T) = \lambda_0^{\text{ref}} - k\log_{10}(T/T^{\text{ref}}) , \quad (B.1)$$

where $\lambda_0^{\text{ref}} = 529.059$ nm, $k = 0.0048$ nm and $T^{\text{ref}} = 280$ eV (see figure B1). We note that, during the velocity inversion procedure, we determine a global offset velocity to account for instrumental drifts of the reference wavelength. The typical range of ion temperature variations from the edge to the core measurement locations (0.2 – 2 keV) in W7-X casts a relative velocity shift of ~2 km/s. Therefore, the effect of including the temperature correction (B.1) is to slightly modify the shape of the inverted velocity profiles (see figure B2).

Appendix B.2. Cross-section and finite-lifetime corrections

In this appendix we derive the expressions used in the article for the corrections to the apparent temperature and velocity that result from the energy dependence of the charge exchange reaction cross-section. The equilibrium kinetic equation for the distribution function of the excited $n = 8$ C^{5+} ions that contribute to the active charge exchange signal,
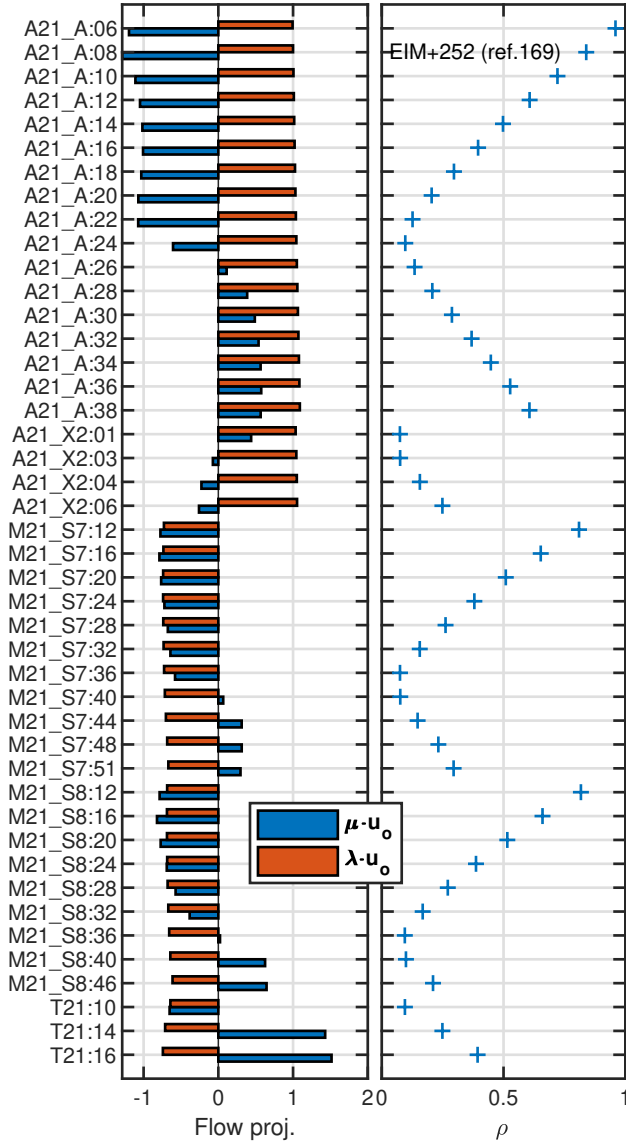
Figure A1. Left: projections of the flow-defining vector fields (A.14) and (A.15) along the observation direction of the multiple CXRS viewing chords. The chords starting A21, M21 and T21 correspond to the toroidal, 45 deg and −45 deg systems respectively. Right: radial localisation of the measurement. The magnetic configuration used for the geometry calculations is the standard EIM (w7x_ref_169).
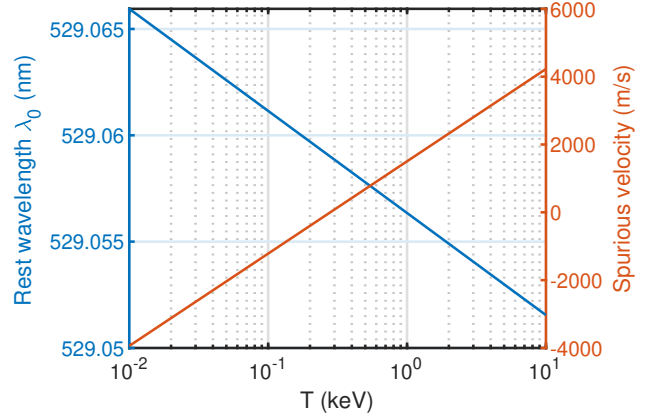

Figure B1. Left: shift of the rest wavelength due to the unresolved fine structure as a function of the ion temperature (cf. figure 8 in [8]). Note that the approximation (B.1) overestimates the wavelength reduction for $T \gtrsim 4\mathrm{keV}$. Right: equivalent 'spurious' velocity resulting from considering λ_0^{ref} as the constant rest wavelength, i.e. $\Delta v = -c(\lambda_0 - \lambda_0^{\mathrm{ref}})/\lambda_0^{\mathrm{ref}}$.

and velocity and Q is the collision-energy-dependent charge exchange reaction rate. The second term on the right hand side represents the radiative decay of the excited carbon with an average lifetime given by ν^{-1}.

We will assume that the spatial scales of f_5^{CX} are large compared to the gyroradius, so that we can neglect the spatial derivative term to get

$$\frac{Ze}{m}(\mathbf{E}+\mathbf{v}\times\mathbf{B})\cdot\nabla_{\mathbf{v}}f_5^{\mathrm{CX}} = n_b Q(|\mathbf{v}-\mathbf{V}_b|)f_6 - \nu f_5^{\mathrm{CX}} \ . \quad (\mathrm{B}.3)$$

Further simplifications of this equation are possible, since the gyrofrequency of C^{5+} ions in the magnetic field of W7-X, $\omega_c = ZeB/m \sim 10^8$ s^{-1}, is small compared to the typical inverse lifetime of the excited state $\nu \sim 10^9$ s^{-1} (see e.g. [36]). This would allow one to neglect the so-called *finite lifetime* effects, dropping the left hand side of equation (B.3) against the radiative decay rate (second term on the right hand side). Nevertheless, we chose to keep those terms as far as possible to keep our expressions general and discuss the simplifications in the final expressions.

Appendix B.2.1. Moments of the equilibrium kinetic equation. In deriving the cross-section and finite lifetime corrections to the apparent CX velocity and temperature measurements we need to relate the measured moments of the CX distribution function f_5^{CX} to those of the unperturbed distribution function of the fully ionised carbon f_6. Taking the zeroth $\int d^3\mathbf{v}(\cdot)$ moment of equation (B.3) we get

$$n_{\mathrm{CX}} = \frac{n_b}{\nu}\int d^3\mathbf{v}\, Q(|\mathbf{v}-\mathbf{V}_b|)f_6(\mathbf{v}) \ , \quad (\mathrm{B}.4)$$

where $n_{\mathrm{CX}} = \int d^3\mathbf{v}\, f_5^{\mathrm{CX}}$ is the density of C^{5+} ions that contribute to the active CX signal. The first moment

that we denote $f_5^{\mathrm{CX}}(\mathbf{x}, \mathbf{v})$, is

$$\mathbf{v}\cdot\nabla f_5^{\mathrm{CX}} + \frac{Ze}{m}(\mathbf{E}+\mathbf{v}\times\mathbf{B})\cdot\nabla_{\mathbf{v}}f_5^{\mathrm{CX}} =$$
$$n_b Q(|\mathbf{v}-\mathbf{V}_b|)f_6 - \nu f_5^{\mathrm{CX}} \ . \quad (\mathrm{B}.2)$$

All variables on the left hand side of this equation have their usual meaning (see. e.g. [19]). The first term on the right hand side represents the source of excited hydrogen-like carbon that results from charge exchange reactions with the neutral beam ions. Here $f_6(\mathbf{x}, \mathbf{v})$ is the distribution function of the fully ionised carbon, n_b and $\mathbf{V}_b$ are the neutral beam ion density

$\int d^3\mathbf{v}\, \mathbf{v}(\cdot)$ gives

$$-\frac{Zen_{\mathrm{CX}}}{m}\left(\mathbf{E} + \mathbf{V}_{\mathrm{CX}} \times \mathbf{B}\right) =$$
$$n_b \int d^3\mathbf{v}\, Q(|\mathbf{v} - \mathbf{V}_b|)\mathbf{v}f_6 - \nu n_{\mathrm{CX}}\mathbf{V}_{\mathrm{CX}} \tag{B.5}$$

where $\mathbf{V}_{\mathrm{CX}} = n_{\mathrm{CX}}^{-1} \int d^3\mathbf{v}\ \mathbf{v}f_5^{\mathrm{CX}}$ is the apparent velocity. Finally, introducing the velocity along the direction of observation, with unitary vector $\mathbf{u}_o$, $v_o = \mathbf{v}\cdot\mathbf{u}_o$ and taking the second order moment $\int d^3\mathbf{v}\, mv_o^2(\cdot)$ gives

$$-2Zen_{\mathrm{CX}}\mathbf{E}\cdot\mathbf{V}_{\mathrm{CX}o}$$
$$-2ZeB\int d^3\mathbf{v}\, v_o(\mathbf{v}\cdot\mathbf{b}\times\mathbf{u}_o)f_5^{\mathrm{CX}} =$$
$$n_b\int d^3\mathbf{v}\, Q(|\mathbf{v}-\mathbf{V}_b|)mv_o^2 f_6 - \nu n_{CX}T_{\mathrm{CX}o}\ . \tag{B.6}$$

where $T_{\mathrm{CX}o} = n_{\mathrm{CX}}^{-1}\int d^3\mathbf{v}\ mv_o^2 f_5^{\mathrm{CX}}$ is the apparent temperature along the direction of observation and $\mathbf{V}_{\mathrm{CX}o} = (\mathbf{V}_{\mathrm{CX}}\cdot\mathbf{u}_o)\mathbf{u}_o$.

Now, one would like to explicitly relate the apparent velocity $\mathbf{V}_{\mathrm{CX}}$ and temperature $T_{\mathrm{CX}o}$ to the real velocity and temperature of the fully stripped carbon, namely $\mathbf{V} = n^{-1}\int d^3\mathbf{v}\ \mathbf{v}f_6$ and $T = n^{-1}\int d^3\mathbf{v}\ mv_o^2 f_6$, with $n = \int d^3\mathbf{v}\ f_6$. For that we expand the reaction rate Q around the impact energy of the neutral beam ions keeping only the leading order corrections. In fact, in most conditions of practical interest the velocity of the neutral beam ions is much larger than the thermal velocity of impurities, i.e.,

$$V_b^2 = 2E_b \gg \frac{2T}{m} = v_t^2\ , \tag{B.7}$$

where E_b is the kinetic energy of the injected neutrals per unit mass. Its nominal value for the NBI injectors at W7-X is 60 keV/amu. We take the reaction rate Q for the reaction $H^0 + C^{6+} \rightarrow H^+ + C^{5+}(n = 8)$ to be a function to the energy of the collision per unit mass $E = \frac{1}{2}(\mathbf{v} - \mathbf{V}_b)^2 = \frac{1}{2}V_b^2 + \left(\frac{1}{2}v^2 - \mathbf{v}\cdot\mathbf{V}_b\right)$ and expand in $\epsilon = \frac{1}{2}v^2 - \mathbf{v}\cdot\mathbf{V}_b \ll \frac{1}{2}V_b^2$,

$$Q\left(\frac{1}{2}(\mathbf{v}-\mathbf{V}_b)^2\right) = Q_b + \epsilon Q_b' + \frac{1}{2}\epsilon^2 Q_b'' + \circ(\epsilon^3)$$
$$= Q_b - \mathbf{v}\cdot\mathbf{V}_b Q_b' + \frac{1}{2}v^2 Q_b' + \tag{B.8}$$
$$+ \frac{1}{2}(\mathbf{v}\cdot\mathbf{V}_b)^2 Q_b'' + \circ(v^3)\ ,$$

where $Q_b = Q(E_b)$ and prime denotes the derivative with respect to E. The density of the CX distribution function is, from (B.4), approximated by $n_{\mathrm{CX}} = (n_b Q_b/\nu)n$.

Appendix B.2.2. Corrections to the velocity If we now substitute the expansion (B.8) in the Q integral in

(B.5) we get

$$\int d^3\mathbf{v}\, n_b Q\left(\frac{1}{2}(\mathbf{v}-\mathbf{V}_b)^2\right)\mathbf{v}f_6(\mathbf{v})$$
$$\approx n_b\int d^3\mathbf{v}\, (Q_b - (\mathbf{v}\cdot\mathbf{V}_b)Q_b')\mathbf{v}f_6(\mathbf{v}) \tag{B.9}$$
$$= n_b Q_b n\mathbf{V} - n_b Q_b' n\frac{T}{m}\mathbf{V}_b\ ,$$

where, in the second term, we have assumed that the distribution function f_6 is approximately centred $(mV^2 \ll T)$.

We note that, in practice, there are several sources of excited carbon produced by the beam injection in the left-hand side of (B.2). These include the several energy components of the beam (full, half and third acceleration voltage) and possibly halo neutrals[+]. The factor $n_b Q_b$ needs then to be replaced by $\sum_b n_b Q_b$ and (B.5) reads

$$\mathbf{V}_{\mathrm{CX}} - \frac{\omega_c}{\nu}\left(\frac{\mathbf{E}}{B} + \mathbf{V}_{\mathrm{CX}}\times\mathbf{b}\right) =$$
$$\mathbf{V} - \frac{T}{m}\sum_b w_b \frac{Q_b'}{Q_b}\mathbf{V}_b\ , \tag{B.10}$$

where the component weight is defined as $w_b = n_b Q_b / \sum_b n_b Q_b$ and measures the relative contribution of the process to the CXRS signal. Note that the correction associated to the halo neutrals is 0, for their thermal velocity is much greater than their possible fluid velocity.

Equation (B.10) relates the apparent velocity vector at a point to the real velocity vector. The measurements give the projection of the apparent velocity in the direction of observation, $V_{\mathrm{CX}o} = \mathbf{V}_{\mathrm{CX}} \cdot \mathbf{u}_o$. If the ratio of gyrofrequency to decay rate of the excited state ω_c/ν is not small, recovering the projection of the actual velocity $V_o = \mathbf{V}\cdot\mathbf{u}_o$ would require to measure all three components of the apparent velocity at that point, according to (B.10). If, on the contrary, $\omega_c/\nu \ll 1$, then the second term on the left-hand side of this equation can be considered a smaller correction compared to the potentially large apparent shift of velocity caused by the second term on the right-hand side. For typical W7-X parameters the second term of the right-hand side of (B.10) can be of the order of 20 km/s in the direction of the beam, which is larger than the expected fluid velocity of C^{6+} ions $\mathbf{V}$. Then, for $\omega_c/\nu \ll 1$

$$\mathbf{V}_{\mathrm{CX}} \approx \mathbf{V} - \frac{T}{m}\sum_b w_b \frac{Q_b'}{Q_b}\mathbf{V}_b\ , \tag{B.11}$$

[+] The various excitation states of the neutrals in the halo and the beam components are considered different sources, for they have different cross sections for the charge transfer reactions with C^{6+}. In cases of practical relevance in W7-X the signal is split between ground state beam neutrals with full and half energy and excited $n = 2$ halo neutrals (see section 2)
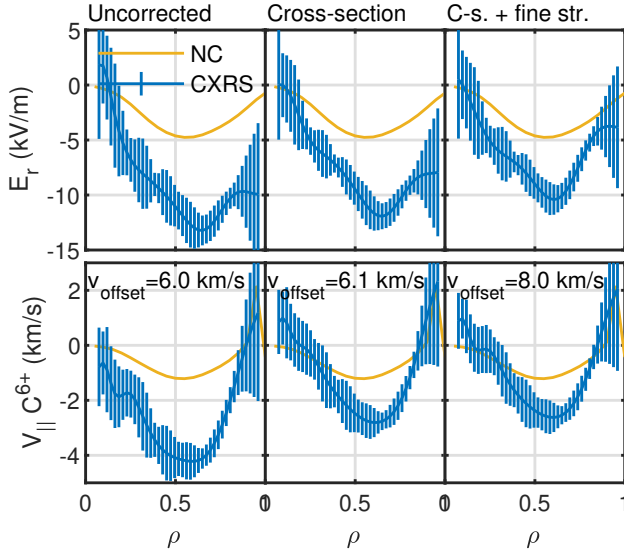
Figure B2. Illustration of the effects of the velocity corrections on the inverted flow profiles for the inversion shown in figure 10. The plots in the left column show the inversion without any consideration of cross-section, finite lifetime or fine structure corrections. Those in the second columns include cross-section and finite lifetime corrections (as from (B.12)). The right column plots include additionally the fine structure corrections (B.1).

The observations are generally done at an approximately right angle with respect to the beam injection, which reduces the effect of this correction on the measurement. However, even for an observation that is perfectly perpendicular to the beam one needs to assess the potential influence of the beam velocity through the $\mathbf{V}_{CX} \times \mathbf{b}$ term, especially if the zero lifetime condition $\omega_c/\nu \ll 1$ is not very well satisfied (for the W7-X field $\omega_c/\nu \sim 0.1$). To estimate the finite lifetime effect we approximate $\mathbf{V}_{CX}$ by its zero-lifetime approximation (B.11) in the second term on the left-hand side of (B.10) to get

$$\mathbf{V}_{CX} \approx \mathbf{V} - \frac{T}{m} \sum_b w_b \frac{Q_b'}{Q_b} \left(\mathbf{V}_b + \frac{\omega_c}{\nu} \mathbf{V}_b \times \mathbf{b} \right) , \quad (B.12)$$

where we have neglected corrections of the size $\frac{\omega_c}{\nu} V$ and used $E/B \sim V$. This expression is used in this work to evaluate cross-section and finite lifetime velocity corrections. We note that, with the ratio of gyrofrequency to decay rate characteristic of W7-X plasmas ($\omega_c/\nu \sim 0.1$) and the viewing geometry of the fibre arrays, finite lifetime corrections are much smaller than their cross-section counterparts.

Appendix B.2.3. Corrections to the temperature The Q term in (B.6) can now be estimated using (B.8) and a Maxwellian form for the distribution function

$$f_6 = \frac{n}{2\pi^{3/2} v_t^3} \exp\left(-\frac{mv^2}{2T}\right),$$

$$\int d^3\mathbf{v} \, n_b Q\left(\frac{1}{2}(\mathbf{v}-\mathbf{V}_b)^2\right) mv_o^2 f_6(\mathbf{v}) \approx$$

$$n_b Q_b nT + \frac{5}{2} n_b Q_b' \frac{T}{m} nT + \qquad (B.13)$$

$$+ n_b Q_b'' \frac{V_b^2}{2} \frac{T}{m} \left(1 + 2(\mathbf{u}_o \cdot \mathbf{u}_b)^2\right) nT .$$

Using this in equation (B.6), neglecting the terms in the left-hand side and reordering one gets

$$T_{CXo} = T(1+\alpha) \qquad (B.14)$$

where

$$\alpha = \sum_b w_b \left(\frac{5}{2} \frac{Q_b'}{Q_b} + \frac{Q_b'' E_b}{Q_b}(1 + 2(\mathbf{u}_o \cdot \mathbf{u}_b)^2)\right) \frac{T}{m} , (B.15)$$

and b runs through the various energy components in the beam. We note that the terms in the LHS of equation (B.6) are of order $\omega_c m n_{CX} V_{CX}^2$, that is, much smaller than those in the RHS ($\sim \nu n_{CX} T_{CX}$) even for $\omega_c \gtrsim \nu$: finite lifetime corrections are of potential importance only for the CXRS velocity. For cases of practical relevance in W7-X the relative temperature corrections resulting from (B.14) are small ($\lesssim 1\%$) and have not been considered in this study.

Appendix C. Expressions for the reaction rates from cross-section data

In this section we provide the formulas used for the calculation of reaction rates

$$n_1 n_2 \langle \sigma v \rangle_{1,2} = \int d^3\mathbf{v} d^3\mathbf{v}' Q(|\mathbf{v}-\mathbf{v}'|) f_1(\mathbf{v}) f_2(\mathbf{v}') , (C.1)$$

from cross section σ, where $Q(\mathbf{v}-\mathbf{v}') = \sigma(|\mathbf{v}-\mathbf{v}'|)|\mathbf{v}-\mathbf{v}'|$. We consider the cases of two colliding Maxwellian distributions and for the case of a collimated mono-energetic beam colliding with a Maxwellian distribution.

Two Maxwellian populations. For the first case we have

$$\langle \sigma v \rangle = \frac{1}{\pi^3 v_{t1}^3 v_{t2}^3} \int_{-\infty}^{\infty} d^3\mathbf{v} d^3\mathbf{v}' Q(|\mathbf{v}-\mathbf{v}'|) e^{-\frac{v^2}{v_{t1}^2}} e^{-\frac{v'^2}{v_{t2}^2}} .$$

Normalising the velocities by the respective thermal velocity (i.e. $\mathbf{v}/v_{t1} \to \mathbf{v}$ and $\mathbf{v}'/v_{t2} \to \mathbf{v}'$) and defining $\mathbf{u} = (v_{t1}\mathbf{v} - v_{t2}\mathbf{v}')/v_{t1}$ and $\alpha = v_{t1}/v_{t2}$ one gets

$$\langle \sigma v \rangle = \frac{\alpha^3}{\pi^3} \int d^3\mathbf{v} d^3\mathbf{u} \, Q(v_{t1}u) e^{-v^2} e^{-\alpha^2|\mathbf{v}-\mathbf{u}|^2}$$

$$= \frac{\alpha^3}{\pi^3} \int d^3\mathbf{u} \, Q(v_{t1}u) e^{-\alpha^2 u^2} I(u) ,$$

where

$$I(u) = \int d^3\mathbf{v} \, e^{-(1+\alpha^2)v^2} e^{2\alpha^2 \mathbf{u}\cdot\mathbf{v}}$$

$$= \frac{\pi^{3/2}}{(1+\alpha^2)^{3/2}} e^{\frac{\alpha^4}{1+\alpha^2} u^2} .$$

Finally

$$\langle\sigma v\rangle = \frac{4}{\sqrt{\pi}}\frac{\alpha^3}{(1+\alpha^2)^{3/2}}\int_0^\infty du\, u^2 Q(v_{t1}u)e^{-\frac{\alpha^2 u^2}{1+\alpha^2}}\ ,$$

or, equivalently,

$$\langle\sigma v\rangle = \frac{4}{\sqrt{\pi}}\int_0^\infty du\, u^2 Q\left(u\sqrt{v_{t1}^2+v_{t2}^2}\right)e^{-u^2}\ . \quad (C.2)$$

Collimated mono-energetic beam colliding with a Maxwelllian distribution. The velocity distribution of the beam neutrals can be approximated by a Dirac's delta function $f_b(\mathbf{v}) = n_b\delta^3(\mathbf{v}-\mathbf{V}_b)$ so that

$$\langle\sigma v\rangle = \frac{1}{\pi^{3/2}v_t^3}\int_{-\infty}^\infty d^3\mathbf{v}\, Q(|\mathbf{v}-\mathbf{V}_b|)e^{-\frac{v^2}{v_t^2}}$$
$$= \frac{e^{-U_b^2}}{\pi^{3/2}}\int_{-\infty}^\infty d^3\mathbf{u}\, Q(v_t u)e^{-(u^2+2\mathbf{u}\cdot\mathbf{U}_b)}\ ,$$

where $\mathbf{u} = (\mathbf{v}-\mathbf{V}_b)/v_t$ and $\mathbf{U}_b = \mathbf{V}_b/v_t$. Integrating the angular variables in spherical coordinates yields

$$\langle\sigma v\rangle = \frac{2e^{-U_b^2}}{U_b\sqrt{\pi}}\int_0^\infty du\, uQ(v_t u)\sinh(2uU_b)e^{-u^2}\ . \quad (C.3)$$

In the limit $U_b \ll 1$, this expression reduces to (C.2) in the limit $v_{t1} \gg v_{t2}$. The expression (C.3) can be rewritten as

$$\langle\sigma v\rangle = \frac{1}{U_b\sqrt{\pi}}\int_0^\infty du\, uQ(v_t u)\left(e^{-(u-U_b)^2}-e^{-(u+U_b)^2}\right)\ ,$$

from which it is simple to see that $\langle\sigma v\rangle \to Q(V_b)$ when the beam velocity is much greater than the thermal velocity of the target particles, $U_b \gg 1$.

References

[1] J. Arévalo et al. "Compressible impurity flow in the TJ-II stellarator". In: *Nuclear Fusion* 54.1 (2014), p. 013008. URL: http://stacks.iop.org/0029-5515/54/i=1/a=013008.

[2] J. Arévalo et al. "Incompressibility of impurity flows in low density TJ-II plasmas and comparison with neoclassical theory". In: *Nuclear Fusion* 53.2 (2013), p. 023003. URL: http://stacks.iop.org/0029-5515/53/i=2/a=023003.

[3] J Baldzuhn et al. "Enhanced energy confinement after series of pellets in Wendelstein 7-X". In: *Plasma Physics and Controlled Fusion* 62.5 (2020), p. 055012. DOI: 10.1088/1361-6587/ab8112. URL: https://doi.org/10.1088%2F1361-6587%2Fab8112.

[4] J Baldzuhn et al. "Measurement and calculation of the radial electric field in the stellarator W7-AS". In: *Plasma Physics and Controlled Fusion* 40.6 (1998), pp. 967–986. DOI: 10.1088/0741-3335/40/6/006. URL: https://doi.org/10.1088%2F0741-3335%2F40%2F6%2F006.

[5] C.D. Beidler et al. "Benchmarking of the mono-energetic transport coefficients—results from the International Collaboration on Neoclassical Transport in Stellarators (ICNTS)". In: *Nuclear Fusion* 51.7 (2011), p. 076001. URL: http://stacks.iop.org/0029-5515/51/i=7/a=076001.

[6] CD Beidler et al. "Demonstration of reduced neoclassical energy transport in Wendelstein 7-X". In: *Nature* 596.7871 (2021), pp. 221–226. DOI: 10.1038/s41586-021-03687-w. URL: https://doi.org/10.1038/s41586-021-03687-w.

[7] R. E. Bell and E. J. Synakowski. "New understanding of poloidal rotation measurements in a Tokamak plasma". In: *AIP Conference Proceedings* 547.1 (2000), pp. 39–52. DOI: 10.1063/1.1361778. URL: https://aip.scitation.org/doi/abs/10.1063/1.1361778.

[8] A Blom and C Jupén. "Parametrization of the Zeeman effect for hydrogen-like spectra in high-temperature plasmas". In: *Plasma Physics and Controlled Fusion* 44.7 (2002), pp. 1229–1241. DOI: 10.1088/0741-3335/44/7/312. URL: https://doi.org/10.1088%2F0741-3335%2F44%2F7%2F312.

[9] S.A. Bozhenkov et al. "High-performance plasmas after pellet injections in Wendelstein 7-X". In: *Nuclear Fusion* 60.6 (2020), p. 066011. DOI: 10.1088/1741-4326/ab7867. URL: https://doi.org/10.1088/1741-4326/ab7867.

[10] A Briesemeister et al. "Comparison of the flows and radial electric field in the HSX stellarator to neoclassical calculations". In: *Plasma Physics and Controlled Fusion* 55.1 (2012), p. 014002. DOI: 10.1088/0741-3335/55/1/014002. URL: https://doi.org/10.1088%2F0741-3335%2F55%2F1%2F014002.

[11] D. Carralero et al. "Characterization of the radial electric field and edge velocity shear in Wendelstein 7-X". In: *Nuclear Fusion* 60.10 (2020), p. 106019. DOI: 10.1088/1741-4326/ab9885. URL: https://doi.org/10.1088/1741-4326/ab9885.

[12] J. Chen et al. "Effect of energy dependent cross-section on flow velocity measurements with charge exchange spectroscopy in magnetized plasma". In: *Physics Letters A* 383 (Apr. 2019). DOI: 10.1016/j.physleta.2019.01.032.

[13] A. Dinklage et al. "Inter-machine validation study of neoclassical transport modelling in medium- to high-density stellarator-heliotron plasmas". In: *Nuclear Fusion* 53.6 (2013), p. 063022. DOI: 10.1088/0029-5515/53/6/

063022. URL: `https://doi.org/10.1088%2F0029-5515%2F53%2F6%2F063022`.

[14] Andreas Dinklage et al. "Magnetic configuration effects on the Wendelstein 7-X stellarator". In: *Nature Physics* 14.8 (2018), pp. 855–860. DOI: `10.1038/s41567-018-0141-9`. URL: `https://doi.org/10.1038/s41567-018-0141-9`.

[15] Teresa Estrada et al. "Radial electric field and density fluctuations measured by Doppler reflectometry during the post-pellet enhanced confinement phase in W7-X". In: *Nuclear Fusion* (2021). URL: `http://iopscience.iop.org/article/10.1088/1741-4326/abddee`.

[16] O. P. Ford et al. "Charge exchange recombination spectroscopy at Wendelstein 7-X". In: *Review of Scientific Instruments* 91.2 (2020), p. 023507. DOI: `10.1063/1.5132936`. eprint: `https://doi.org/10.1063/1.5132936`. URL: `https://doi.org/10.1063/1.5132936`.

[17] J Geiger et al. "Physics in the magnetic configuration space of W7-X". In: *Plasma Physics and Controlled Fusion* 57.1 (2014), p. 014004. DOI: `10.1088/0741-3335/57/1/014004`. URL: `https://doi.org/10.1088/0741-3335/57/1/014004`.

[18] G. Grieger et al. "Physics optimization of stellarators". In: *Physics of Fluids B: Plasma Physics* 4.7 (1992), pp. 2081–2091. DOI: `10.1063/1.860481`. eprint: `https://doi.org/10.1063/1.860481`. URL: `https://doi.org/10.1063/1.860481`.

[19] Richard D Hazeltine and François L Waelbroeck. *The Framework of Plasma Physics*. Frontiers in Physics. Boulder, CO: Westview, 2004.

[20] M von Hellermann et al. "Analytical approximation of cross-section effects on charge exchange spectra observed in hot fusion plasmas". In: *Plasma Physics and Controlled Fusion* 37.2 (1995), pp. 71–94. DOI: `10.1088/0741-3335/37/2/002`. URL: `https://doi.org/10.1088%2F0741-3335%2F37%2F2%2F002`.

[21] R. B. Howell et al. "Corrections to charge exchange spectroscopic measurements in TFTR due to energy-dependent excitation rates". In: *Review of Scientific Instruments* 59.8 (1988), pp. 1521–1523. DOI: `10.1063/1.1140183`. URL: `https://doi.org/10.1063/1.1140183`.

[22] R. K. Janev, D. Reiter, and U. Samm. *Collision Proecesses in Low-Temperature Hydrogen Plasmas*. Tech. rep. 4105. Forschungzentrum Jülich, 1999.

[23] T. Klinger et al. "Overview of first Wendelstein 7-X high-performance operation". In: *Nuclear Fusion* 59.11 (2019), p. 112004. DOI: `10.1088/1741-4326/ab03a7`. URL: `https://doi.org/10.1088/1741-4326/ab03a7`.

[24] A. Krämer-Flecken et al. "Investigation of turbulence rotation in limiter plasmas at W7-X with newly installed poloidal correlation reflectometer". In: *Nuclear Fusion* 57.6 (2017), p. 066023. DOI: `10.1088/1741-4326/aa66ae`. URL: `https://doi.org/10.1088/1741-4326/aa66ae`.

[25] S. Äkäslompolo et al. "Validating the ASCOT modelling of NBI fast ions in Wendelstein 7-X stellarator". In: *Journal of Instrumentation* 14.10 (2019), pp. C10012–C10012. DOI: `10.1088/1748-0221/14/10/c10012`. URL: `https://doi.org/10.1088/1748-0221/14/10/c10012`.

[26] S T A Kumar et al. "Radial electric field and ion parallel flow in the quasi-symmetric and Mirror configurations of HSX". In: *Plasma Physics and Controlled Fusion* 60.5 (2018), p. 054012. DOI: `10.1088/1361-6587/aab4c7`. URL: `https://doi.org/10.1088%2F1361-6587%2Faab4c7`.

[27] S.T.A. Kumar et al. "Determination of radial electric field from Pfirsch–Schlüter flows in the HSX stellarator". In: *Nuclear Fusion* 57.3 (2017), p. 036030. DOI: `10.1088/1741-4326/aa52a2`. URL: `https://doi.org/10.1088%2F1741-4326%2Faa52a2`.

[28] M. Landreman et al. "Comparison of particle trajectories and collision operators for collisional transport in nonaxisymmetric plasmas". In: *Physics of Plasmas (1994-present)* 21.4, 042503 (2014), pp. –. DOI: `http://dx.doi.org/10.1063/1.4870077`. URL: `http://scitation.aip.org/content/aip/journal/pop/21/4/10.1063/1.4870077`.

[29] H. Maaßberg, C. D. Beidler, and Y. Turkin. "Momentum correction techniques for neoclassical transport in stellarators". In: *Physics of Plasmas* 16.7 (2009), p. 072504. DOI: `10.1063/1.3175328`. eprint: `https://doi.org/10.1063/1.3175328`. URL: `https://doi.org/10.1063/1.3175328`.

[30] K D Marr et al. "Comparison of neoclassical predictions with measured flows and evaluation of a poloidal impurity density asymmetry". In: *Plasma Physics and Controlled Fusion* 52.5 (2010), p. 055010. URL: `http://stacks.iop.org/0741-3335/52/i=5/a=055010`.

[31] R M McDermott et al. "Evaluation of impurity densities from charge exchange recombination spectroscopy measurements at ASDEX Upgrade". In: *Plasma Physics and Controlled Fusion* 60.9 (2018), p. 095007. DOI: 10.1088/1361-6587/aad256. URL: https://doi.org/10.1088%2F1361-6587%2Faad256.

[32] K. Nagaoka et al. "3-D effects on viscosity and generation of toroidal and poloidal flows in LHD". In: *Physics of Plasmas* 20.5 (2013), p. 056116. DOI: 10.1063/1.4807126. URL: https://doi.org/10.1063/1.4807126.

[33] N. A. Pablant et al. "Core radial electric field and transport in Wendelstein 7-X plasmas". In: *Physics of Plasmas* 25.2 (2018), p. 022508. DOI: 10.1063/1.4999842. eprint: https://doi.org/10.1063/1.4999842. URL: https://doi.org/10.1063/1.4999842.

[34] T. Pütterich et al. "Poloidal asymmetry of parallel rotation measured in ASDEX Upgrade". In: *Nuclear Fusion* 52.8 (2012), p. 083013. URL: http://stacks.iop.org/0029-5515/52/i=8/a=083013.

[35] W. I. van Rij and S. P. Hirshman. "Variational bounds for transport coefficients in three-dimensional toroidal plasmas". In: *Physics of Fluids B: Plasma Physics* 1.3 (1989), pp. 563–569. DOI: 10.1063/1.859116. eprint: https://doi.org/10.1063/1.859116. URL: https://doi.org/10.1063/1.859116.

[36] W. M. Solomon et al. "Extraction of poloidal velocity from charge exchange recombination spectroscopy measurements". In: *Review of Scientific Instruments* 75.10 (2004), pp. 3481–3486. DOI: 10.1063/1.1790042. eprint: https://doi.org/10.1063/1.1790042. URL: https://doi.org/10.1063/1.1790042.

[37] Annabelle Spanier et al. "Performance of the first neutral beam injector at the Wendelstein 7-X stellarator". In: *Fusion Engineering and Design* 163 (2021), p. 112115. ISSN: 0920-3796. DOI: https://doi.org/10.1016/j.fusengdes.2020.112115. URL: https://www.sciencedirect.com/science/article/pii/S0920379620306633.

[38] M. Taguchi. "A method for calculating plasma rotation velocity due to internal and external sources". In: *Physics of Plasmas* 18.10 (2011), p. 102505. DOI: 10.1063/1.3651769. eprint: https://doi.org/10.1063/1.3651769. URL: https://doi.org/10.1063/1.3651769.

[39] J.L. Velasco et al. "KNOSOS: A fast orbit-averaging neoclassical code for stellarator geometry". In: *Journal of Computational Physics* 418 (2020), p. 109512. ISSN: 0021-9991. DOI: https://doi.org/10.1016/j.jcp.2020.109512. URL: https://www.sciencedirect.com/science/article/pii/S0021999120302862.

[40] J.L. Velasco et al. "Moderation of neoclassical impurity accumulation in high temperature plasmas of helical devices". In: *Nuclear Fusion* 57.1 (2017), p. 016016. URL: http://stacks.iop.org/0029-5515/57/i=1/a=016016.

[41] W. L. Wiese and J. R. Fuhr. "Accurate Atomic Transition Probabilities for Hydrogen, Helium, and Lithium". In: *Journal of Physical and Chemical Reference Data* 38.3 (2009), pp. 565–720. DOI: 10.1063/1.3077727. URL: https://doi.org/10.1063/1.3077727.

[42] T Windisch et al. "Poloidal correlation reflectometry at W7-X: radial electric field and coherent fluctuations". In: *Plasma Physics and Controlled Fusion* 59.10 (2017), p. 105002. DOI: 10.1088/1361-6587/aa759b. URL: https://doi.org/10.1088/1361-6587/aa759b.

[43] R. C. Wolf et al. "Performance of Wendelstein 7-X stellarator plasmas during the first divertor operation phase". In: *Physics of Plasmas* 26.8 (2019), p. 082504. DOI: 10.1063/1.5098761. eprint: https://doi.org/10.1063/1.5098761. URL: https://doi.org/10.1063/1.5098761.

[44] Y. Yamamoto et al. "Effect of the Pfirsch–Schlüter flow on the inboard/outboard asymmetry of the toroidal flow in LHD". In: *Physics of Plasmas* 27.4 (2020), p. 042514. DOI: 10.1063/1.5126526. URL: https://doi.org/10.1063/1.5126526.